J. Fluid Mech. (2004), *vol.* 500, *pp.* 283–312.
DOI: 10.1017/S0022112003007286 Printed in the United Kingdom

Nearly symmetric and nearly baroclinic instabilities in the presence of diffusivity. Part 2. Mode structures and energetics

By QIN XU

NOAA/National Severe Storms Laboratory, 1313 Halley Circle, Norman, OK 73069, USA
Qin.Xu@noaa.gov

(Received 13 March 2003 and in revised form 31 August 2003)

The structures and energetics of nearly symmetric modes and nearly baroclinic modes are analysed in detail to examine their instability mechanisms. It is shown that the nearly symmetric modes have their cross-band circulations slanted mainly between the along-band absolute-momentum surface and buoyancy surface of the basic state. Their growth is thus supported mainly by the symmetric-type energy conversion that transports energy from the basic-state along-band velocity and buoyancy to the perturbation along-band velocity and buoyancy, respectively, and then to the cross-band circulation. However, as the band orientations are tilted slightly away from the basic shear, the growth is also assisted by the baroclinic-type energy conversion that transports energy from the basic-state buoyancy to the perturbation buoyancy via the along-band advection and then to the cross-band circulation. When the band orientation is tilted to the warm (or cold) side of the basic shear, the baroclinic-type energy conversion smooths (or sharpens) the near-boundary structures and thus reduces (enhances) the effect of diffusive damping, especially near the non-slip boundaries. This explains why in the presence of diffusivity the symmetric instability yields to the nearly symmetric instability with the band orientation tilted slightly to the warm side of the basic shear. The nearly baroclinic modes transport warm air northward with rising motion and cold air southward with sinking motion, so their growth is supported mainly by the baroclinic-type energy conversion. Since the band orientations are not exactly perpendicular to the basic shear, the growth is also assisted by two additional energy conversions: (i) from the basic-state buoyancy through the cross-band horizontal advection to the perturbation buoyancy; and (ii) from the basic-state along-band velocity to the perturbation along-band velocity. When the band orientation is tilted, by nearly 90° or less, to the warm (or cold) side of the basic shear, the two additional energy conversions smooth (or sharpen) the near-boundary structures and thus reduce (enhance) the effect of diffusive damping, especially near the non-slip boundaries. This explains why the baroclinic instability yields to the warm-side tilted nearly baroclinic instability in the presence of diffusivity.

1. Introduction

In the inviscid and hydrostatic limit, the instabilities of the Eady baroclinic basic state in three-dimensional space is controlled by a single external parameter: the Richardson number Ri (Stone 1966). The presence of diffusivity (viscosity and conductivity) introduces two additional external parameters: the Ekman number

Ek and Prandtl number Pr. For wide ranges of these external parameters ($1/4 < Ri \leqslant 1$, $0.0001 \leqslant Ek \leqslant 0.02$ and $0.5 \leqslant Pr \leqslant 2.0$), normal-mode growth rates were examined in Xu (2003, referred to as part 1 hereafter) as functions of two internal parameters: the horizontal wavelength l and tilt angle α of the mode orientation with respect to the basic shear (measured negative clockwise from the basic-shear direction to the y-direction, that is, to the warm side of basic shear within 90°). The computed growth rate patterns exhibited new features that differ from the inviscid results of Stone (1966, 1970), although all the differences diminish in the inviscid and hydrostatic limit. Major new features can be summarized as follows. (i) When Ek increases from 0 to 0.01 and Ri is between 0.25 and the transitional Richardson number ($Ri^* = 0.95$ in the inviscid limit), the global maximum point in the growth rate pattern shifts away from the symmetric axis ($\alpha = 0$) to the negative side ($\alpha < 0$) and the associated unstable mode changes from purely symmetric to nearly symmetric. (ii) When Ek increases from 0 to 0.01 and Ri is larger than the inviscid transitional Richardson number ($Ri^* = 0.95$), the global maximum point shifts away from the baroclinic axis ($\alpha = -90°$) to the positive side ($\alpha > -90°$) and the associated unstable mode changes from purely baroclinic to nearly baroclinic. The nearly symmetric modes and nearly baroclinic modes are new in the sense that they cannot be fully explained by the classic theories of symmetric and baroclinic instabilities. Their instability mechanisms are largely unexplored, although the energy conversions of nearly symmetric modes with weak diffusivity and weak instability were examined by Miller & Antar (1986). This is the motivation of this paper.

As a sequel to part 1, this paper is intended to examine the structures of the above two types of unstable modes and to study their instability mechanisms and related energetics, so that physical understanding can be obtained for the aforementioned new features in the growth rate patterns. The paper is organized as follows. The next section presents the equations to be used for the analyses and describes the plan of the study. The symmetric modes are examined first in § 3, and then compared with the warm-side tilted modes ($\alpha < 0$) in § 4 and with the cold-side tilted modes ($\alpha > 0$) in § 5. The nearly baroclinic modes are examined in § 6. Volume-averaged energy analyses are presented in § 7. Summary remarks follow in § 8.

2. Equations for the analyses and plan of the study

2.1. *Equations for mode structure analyses*

The non-dimensional system (3.1*a–c*) in part 1 can be rewritten in the following form:

$$\mathrm{D}_t \zeta = G + Ek\mathrm{D}\zeta, \tag{2.1a}$$

$$\mathrm{D}_t v = J(\psi, M) + Ek\mathrm{D}v, \tag{2.1b}$$

$$\mathrm{D}_t b = J(\psi, B) - v\partial_y B + Ek\mathrm{D}b/Pr, \tag{2.1c}$$

where $\mathrm{D}_t \equiv \partial_t + (z - 0.5)\sin\alpha\,\partial_x$, $\zeta \equiv \partial_z u - a^2\partial_x w = \mathrm{D}\psi$, $G \equiv \partial_z v - Ri\partial_x b$, $\mathrm{D} \equiv a^2\partial_x^2 + \partial_z{}^2$, $J(\psi, \bullet) \equiv \partial_x\psi\,\partial_z(\bullet) - \partial_z\psi\,\partial_x(\bullet) = -(u\partial_x + w\partial_z)(\bullet)$, $a \equiv H/L = r\,Ri^{1/2}$ is the aspect ratio, and $r \equiv f/N$ is the ratio between inertial and buoyancy frequencies (see (2.4)–(2.9) of part 1). Here, $M \equiv x + (z - 0.5)\cos\alpha$ is the basic-state along-band absolute-momentum, that is, $fx + V$ scaled by fL, while $B \equiv (x\cos\alpha - y\sin\alpha)/Ri + z +$ constant is the basic-state buoyancy, that is, $g\Theta/\Theta_\circ$ scaled by HN^2.

Note that G is the vorticity generation term in (2.1*a*) that represents a torque (positive for a clockwise rotation) composed of two parts: the buoyancy torque $-Ri\,\partial_x b$

and the inertial-force torque $\partial_z v$, where v represents the cross-band Coriolis force associated with the along-band velocity. In (2.1*b*), $J(\psi, M)$ represents the generation of v due to the cross-band advection of the basic-state M. In (2.1*c*), $J(\psi, B)$ and $-v\partial_y B$ represent the generation of b due to the cross-band advection and along-band advection of the basic-state B, respectively. The slope of the M-surface is $-1/\cos\alpha$ in three-dimensional space as well as in the cross-band vertical plane (x, z). The slope of the B-surface is $1/Ri$ (viewed from the warm side perpendicular to the basic shear) in three-dimensional space, but is $-\cos\alpha/Ri$ in the cross-band vertical plane. It is easy to see that $J(\psi, M)$ is zero when the streamline is parallel to the M-surface, and is positive (or negative) when the streamline is downward and steeper (or less steep) than the M-surface or when the streamline is upward and less steep (or steeper) than the M-surface in the cross-band vertical plane. The sign of $J(\psi, B)$ can be determined by a similar rule. These simple rules will be used for the visual analyses of the mode structures in this paper.

2.2. *Energy equations*

Averaging ψ(2.1*a*), v(2.1*b*) and bRi(2.1*c*) in the horizontal over one wavelength yields the following energy equations:

$$\partial_t K_2 = C_2 + \partial_z F_2 + D_2, \tag{2.2a}$$

$$\partial_t K_v = C_v + \partial_z F_v + D_v, \tag{2.2b}$$

$$\partial_t P_b = C_b + \langle vb\rangle \sin\alpha + \partial_z F_b + D_b, \tag{2.2c}$$

where $\langle(\bullet)\rangle$ denotes the horizontal average of $(\bullet)$, $K_2 = \langle u^2 + a^2 w^2\rangle/2$ is the kinetic energy associated with the cross-band circulation, $K_v = \langle v^2\rangle/2$ is the kinetic energy associated with the along-band velocity perturbation, and $P_b = \langle b^2\rangle Ri/2$ is the potential energy associated with the buoyancy perturbation. On the right-hand side of (2.2), the three energy conversion terms are defined by

$$C_2 \equiv \langle uv\rangle + \langle wb\rangle Ri - \langle uw\rangle \sin\alpha, \tag{2.3a}$$

$$C_v \equiv -\langle uv\rangle - \langle vw\rangle \cos\alpha, \tag{2.3b}$$

$$C_b \equiv -\langle wb\rangle Ri - \langle ub\rangle \cos\alpha; \tag{2.3c}$$

the energy fluxes in the three vertical gradient terms are defined by

$$F_2 \equiv Ek\langle u\partial_z u + a^2 w\partial_z w\rangle - Ri\langle wp\rangle, \tag{2.4a}$$

$$F_v \equiv Ek\langle v\partial_z v\rangle, \tag{2.4b}$$

$$F_b \equiv Ek\langle b\partial_z b\rangle Ri/Pr; \tag{2.4c}$$

and the three energy dissipation terms are defined by

$$D_2 \equiv -Ek\langle a^2(\partial_x u)^2 + (\partial_z u)^2 + a^2[a^2(\partial_x w)^2 + (\partial_z w)^2]\rangle, \tag{2.5a}$$

$$D_v \equiv -Ek\langle a^2(\partial_x v)^2 + (\partial_z v)^2\rangle, \tag{2.5a}$$

$$D_b \equiv -Ek\langle a^2(\partial_x b)^2 + (\partial_z b)^2\rangle Ri/Pr. \tag{2.5a}$$

The periodic lateral boundary condition and integration by parts are used in the derivation of the above results. Equation (2.7*a*) of part 1 is used in the derivation of (2.2*a*).

The energy conversion terms C_v and C_b in (2.3*b*, *c*) are derived from the two generation terms in (2.1*b*, *c*), respectively. The first two terms of C_2 in (2.3*a*) are derived from the generation term G in (2.1*a*), but there is a flux term, $\partial_z\langle\psi v\rangle$, due to the vertical differentiation by parts used in the derivation. This flux term is absorbed

into the last term in (2.4a) by using (2.7a) of part 1. The last term of C_2 in (2.3a) is derived from the advection term in (2.1a) and there is also a flux term which is absorbed into the last term in (2.4a). Since the last term of C_2 is very small (as shown later in figures 14 and 16), the three energy conversion terms in (2.3a–c) can be simply related to the three generation terms in (2.1a–c), respectively. The second term $\langle vb\rangle \sin\alpha$ on the right-hand side of (2.2c) is the potential energy conversion due to the along-band buoyancy advection and can be related to the v-advection term in (2.1c). Because the energy fluxes defined in (2.4) all vanish at the boundaries in either the free-slip or non-slip case, the three energy flux gradient terms in (2.4a–c) make no net contribution to perturbation energy production and thus will not be considered in the energetic analyses in subsequent sections.

Further integrating (2.2) in the vertical gives

$$\partial_t\{K_2\} = \{\langle uv\rangle\} + \{\langle wb\rangle\}Ri - \{\langle uw\rangle\}\sin\alpha + \{D_2\}, \tag{2.6a}$$

$$\partial_t\{K_v\} = -\{\langle uv\rangle\} - \{\langle vw\rangle\}\cos\alpha + \{D_v\}, \tag{2.6b}$$

$$\partial_t\{P_b\} = -\{\langle wb\rangle\}Ri - \{\langle ub\rangle\}\cos\alpha + \{\langle vb\rangle\}\sin\alpha + \{D_b\}, \tag{2.6c}$$

where $\{(\bullet)\}$ denotes the vertical average of $(\bullet)$. The total energy equation is given by the sum of the three equations in (2.6); that is,

$$\partial_t\{E\} = \{C\} + \{D_2 + D_v + D_b\}, \tag{2.7}$$

where $\{E\} = \{K_2 + K_v + P_b\}$ is the volume-averaged total energy, and $\{C\} = \{C_2 + C_v + C_b + \langle vb\rangle \sin\alpha\}$ is the volume-averaged total energy conversion. Because $\langle uv\rangle + \langle wb\rangle Ri$ in C_2 are cancelled by $-\langle uv\rangle$ in C_v and $-\langle wb\rangle Ri$ in C_b, the total energy conversion contains only three components:

$$C = C_{U2} + C_{Vv} + C_{Bb}, \tag{2.8}$$

where $C_{U2} = -\langle uw\rangle \sin\alpha$ is the kinetic energy conversion between the basic flow and perturbation circulation in the cross-band direction, $C_{Vv} = -\langle vw\rangle \cos\alpha$ the kinetic energy conversion between the basic flow and perturbation flow in the along-band direction, and $C_{Bb} = \langle vb\rangle \sin\alpha - \langle ub\rangle \cos\alpha$ is the potential energy conversion between the basic-state buoyancy and perturbation buoyancy. The total energy equation (2.7) is the essentially same as (17) of Miller & Antar (1986) but scaled differently (see § 6.1 of part 1).

2.3. *Plan of the study and mode selection*

As mentioned in the introduction, the growth rate patterns computed in part 1 exhibited two major new features that differ from the inviscid results of Stone (1966, 1970). To understand the first feature, that is, why the global maximum in the growth rate pattern moves to the negative side of the symmetry axis when Ek increases from 0 to 0.01 and Ri is between 0.25 and the transitional Richardson number ($Ri^* = 0.95$ in the inviscid limit), we need to examine the structures of the nearly symmetric modes compared to the symmetric modes. As reflected by this feature, the presence of diffusivity yields not only a scale selection but also an orientation selection for the most unstable mode. The diffusive scale selection is intuitive and well understood. As a finite horizontal wavelength is determined by the scale selection mechanism for the most unstable mode, we can fix the wavelength l and change the orientation angle α to study the orientation selection mechanism. As will be seen in §§ 4 and 5, the growth of the warm-side (or cold-side) tilted mode is maximally supported by the symmetric-type energy conversion plus the baroclinic-type energy conversion in the middle layer (or boundary layers). Since the baroclinic-type energy conversin enhances

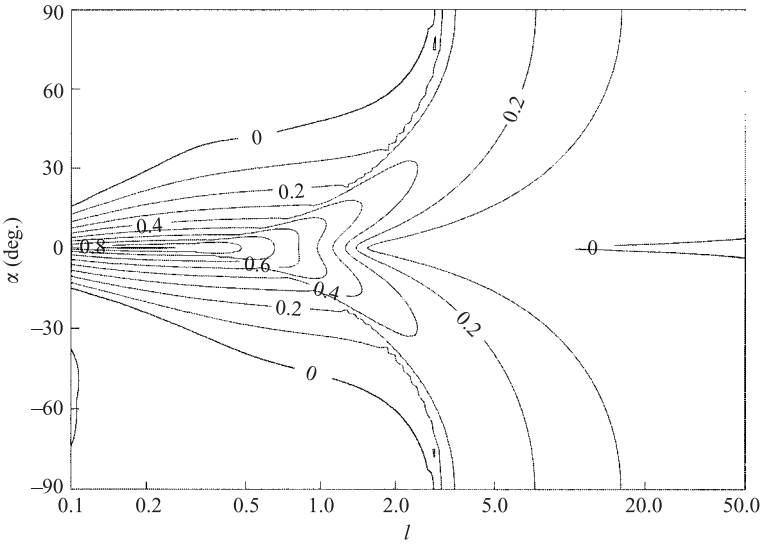

FIGURE 1. Growth rate σ plotted as a function of (l, α) for $\sigma \geqslant 0$ in the non-slip case, where l (plotted in logarithm scale) is the wavelength and α is the tilt angle of the mode orientation (measured negative clockwise from the basic-shear direction to the y-direction, that is, to the warm side of the basic shear). The external parameter values are $Ri = 0.5$, $Ek = 0.0001$, $Pr = 1.0$ and $r^2 = 0.02$. Note that the main growth rate pattern ($\sigma \geqslant 0$ and $\omega = 0$) remains largely the same as that for $Ek = 0.001$ in figure 3 of part 1, but the two side lobes (for the propagating modes) are enlarged by about three times. The maximum growth rate is 0.913 at $(l, \alpha) = (0.186, -0.005°)$.

the middle-layer (or boundary) structures of the warm-side (or cold-side) tilted mode, the mode structures are smoothed (or sharpened) near the boundaries. Hence, the warm-side tilted modes are less severely damped by the increased diffusivity than the cold-side tilted modes. This highlights the physical understanding obtained in this paper for the orientation selection.

For the typical parameter setting ($Ri = 0.5$, $Ek = 0.01$, $Pr = 1.0$ and $r^2 = 0.02$) in figures 1(a) and 2(a) of part 1, the global maxima in the growth rate patterns for the free-slip and non-slip cases are both in the vicinity of $(l, \alpha) = (1, -12°)$, so we can select $(l, \alpha) = (1, -12°)$ and compare the modes at this point with the symmetric modes at $(l, \alpha) = (1, 0)$ and with the modes at $(l, \alpha) = (1, 12°)$ on the positive side of the symmetry axis. With $l = 1$, the dimensional wavelength is given by $L \equiv |\boldsymbol{V}_z| H/f$, that is, the Rossby radius of deformation associated with the basic shear. Since the structure differences between these modes and their implied differences in dynamics are masked by the increased diffusivity ($Ek = 0.01$), it is illuminating to first examine the nearly inviscid mode structures at the points selected above in the parameter space of (l, α) with $Ek = 0.0001$ and then consider the effects of the increased diffusivity. The nearly inviscid growth rate pattern is plotted in figure 1 for the non-slip case with $Ek = 0.0001$ while the remaining external parameter values are as in figure 3 of part 1. The nearly inviscid growth rate pattern for the free-slip case (not shown) is almost identical to that in figure 1 expect for the side lobes (associated with propagating modes). The main growth rate pattern in figure 1 is very close to the inviscid limit (see § 6.2 of part 1).

The growth rate pattern in figure 1 is characterized by a V-shaped ridge with two branches split from a main ridge along the two sides of the symmetry axis. As the

Ekman number increases to 0.01 (see figure 2*a* of part 1), the main ridge collapses, the global maximum point moves along the negative-α branch to the vicinity of the point selected above at $(l, \alpha) = (1, -12^\circ)$, while the positive-$\alpha$ branch drops below zero for the non-slip case but not for the free-slip case (see figures 1*a* and 2*a* of part 1). This implies that the structures of the warm-side tilted modes at $(l, \alpha) = (1, -12^\circ)$ may remain qualitatively the same when Ek increases from 0.0001 to 0.01 regardless of the boundary conditions. This is another reason why we first examine the nearly inviscid mode structures, as mentioned above. For each type of mode selected above, we will examine the nearly inviscid mode structures and related instability mechanisms in a first step, analyse their energetics in a second step, and then consider the effects of the increased diffusivity in a third step. Since the nature of symmetric instability is relatively simple (Xu & Clark 1985) and can be easily interpreted by parcel dynamics (Emanuel 1983) and generalized energetics (Ooyama 1966; Xu 1986), the symmetric modes will be examined first and then compared with the warm-side tilted modes and cold-side tilted modes in the next three sections.

To understand the second major feature summarized in the introduction, that is, why the global maximum in the growth rate pattern shifts away from the baroclinic axis when Ek increases from 0 to 0.01 and Ri is larger than the inviscid transitional Richardson number ($Ri^* = 0.95$), we need to examine the structures of the nearly baroclinic modes compared to the baroclinic modes. For the typical parameter setting ($Ri = 1.0$, $Ek = 0.01$, $Pr = 1.0$ and $r^2 = 0.02$) in figures 1(*e*) and 2(*c*) of part 1, the global maximum growth rates are $\sigma = 0.216$ at $(l, \alpha) = (5.02, -74^\circ)$ for the free-slip case and $\sigma = 0.106$ at $(l, \alpha) = (3.12, -47^\circ)$ for the non-slip case. For the free-slip case, the growth rate pattern is flat in the vicinity of the global maximum and the global maximum is close to the baroclinic axis, so the structure difference between the nearly baroclinic mode and baroclinic mode is small. For the non-slip case, the global maximum is not close to the baroclinic axis, so there is a distinct structure difference between the nearly baroclinic mode and baroclinic mode. The analyses will be focused on the non-slip case. By using the aforementioned three-step approach, the nearly baroclinic mode at $(l, \alpha) = (3.12, -47^\circ)$ will be examined first in §§ 6.1–6.3, and then compared with the baroclinic mode at the conditional maximum point $(l = 3.85, -90^\circ)$ in § 6.4 and with the cold-side tilted mode at $(l, \alpha) = (3.12, 47^\circ)$ in § 6.5.

3. Symmetric modes

3.1. *Mode structures and instability mechanism*

Figure 2 shows the structures of ψ, v, b and G for the non-slip symmetric mode at $(l, \alpha) = (1, 0)$ with $Ek = 0.0001$ and $Ri = 0.5$. To facilitate the later comparisons between different modes, the amplitude of ψ is normalized to unity in figure 2(*a*), where the dashed and solid straight lines are the M-surface and B-surface intersected by the cross-band vertical plane, respectively. As shown by the arrow along the central streamline between the two cells, the slantwise downdraught is steeper than the M-surface but less steep than the B-surface in (x, z). Thus, according to the simple rules stated in § 2.1 $J(\psi, M)$ is positive and $J(\psi, B)$ is negative along the downdraught. Since $\mathrm{D}_t = \partial_t$ and $\partial_y B = 0$ for the symmetric modes, these two terms are the only generation terms in (2.1*b*, *c*). Their generated v is positive and b is negative along the downdraught as shown in figure 2(*b*, *c*). The Coriolis force associated with the positive v is rightward and the buoyancy associated with the negative b is downward. Their combined vector force accelerates the slanted downdraught. The slantwise updraught

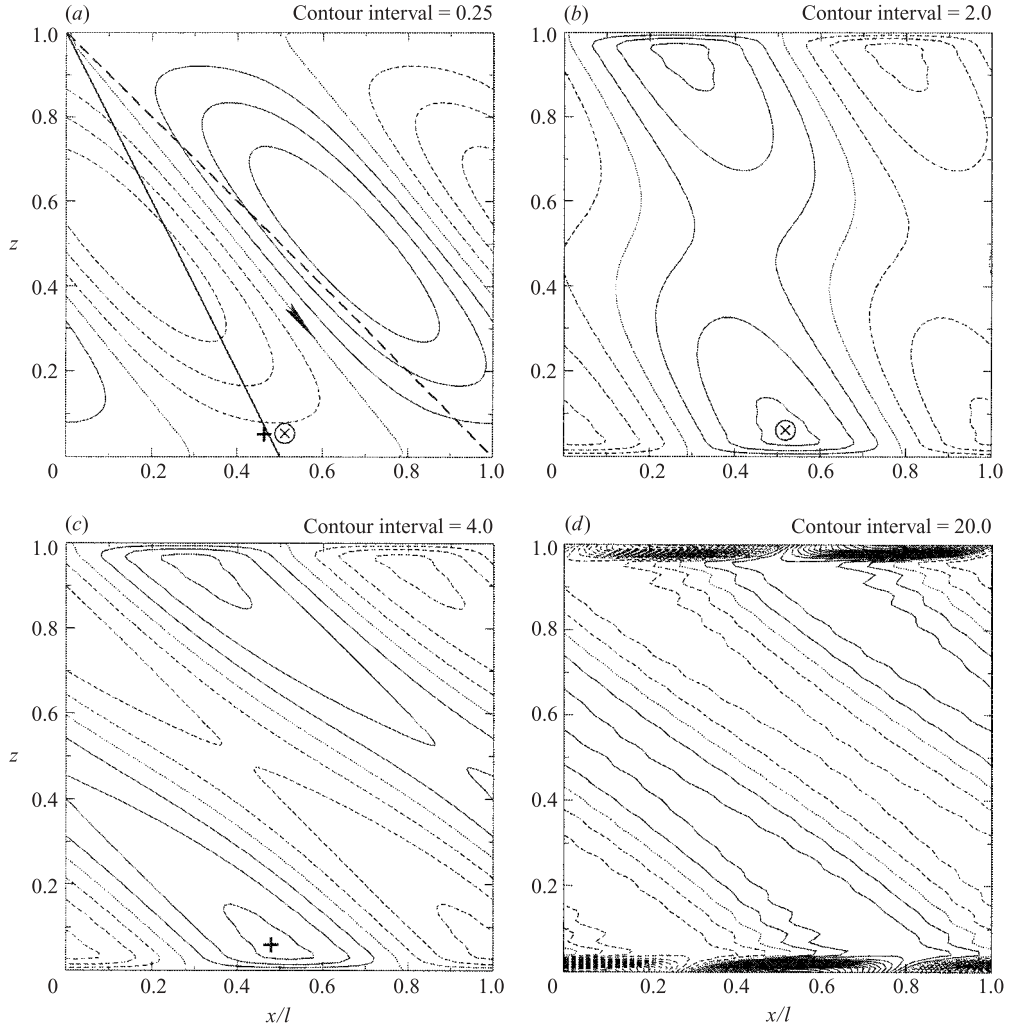

FIGURE 2. Contours (solid for non-negative and dashed for negative) of (*a*) ψ, (*b*) v, (*c*) b, and (*d*) $G = \partial_z v - \partial_x b$ in the cross-band vertical plane $(x/l, z)$ for the non-slip symmetric mode at $(l, \alpha) = (1, 0)$ in figure 1. The horizontal coordinate x is scaled by the wavelength l. The amplitude of ψ is normalized to unity to facilitate comparisons. The amplitudes of v, b and G are 6.6, 13.2 and 330.8, respectively. The growth rate is 0.479. The circulation direction is shown by the arrow along the central streamline between the two cells in (*a*). The positive v-core near the lower boundary is marked by $\otimes$ in (*a*) and (*b*). The positive b-core near the lower boundary is marked by $+$ in (*a*) and (*c*). The dashed and solid straight lines are M-surface and B-surface intersected by the cross-band vertical plane, respectively.

is accelerated similarly by this type of positive feedback. The overall positive feedback is indicated by the positive correlation between the vorticity and vorticity generation or, equivalently, by the negative correlation between ψ and G in the interior domain (figure 2*a*, *d*).

As shown in figure 2(*a*), the slanted downdraught splits into two branches as it approaches the lower boundary. Along the leftward branch, the cross-band advections of the basic-state M and B reach their maxima near the lower boundary between the two stagnation points. These maxima (of $J(\psi, M)$ and $J(\psi, B)$) are marked by $\otimes$

and +, respectively, in figure 2(*a*). The positive *v*-core and *b*-core they produce are marked by ⊗ in figure 2(*b*) and by + in figure 2(*c*), respectively. As the cross-band flow produces the *v*-core, it is decelerated locally by the Coriolis force associated with the *v*-core.

Underneath the positive *v*-core marked by ⊗ in figure 2(*b*), $\partial_z v$ is maximized and so is the vorticity generation. This is shown by the very shallow and intense *G*-cores along the boundaries in figure 2(*d*). These *G*-cores are caused by the non-slip boundary conditions. When the non-slip boundary conditions are replaced by the free-slip ones or the Ekman number becomes zero, the *v*-cores and *b*-cores are shifted onto the boundaries and the shallow *G*-cores mostly diminish. The interior fields, however, remain almost exactly the same as in figure 2.

3.2. *Energy analysis*

Vertical profiles of the energy terms defined in (2.2)–(2.5) are plotted in figure 3 for the non-slip symmetric mode in figure 2. As shown by the solid profile in figure 3(*a*), C_2 is positive in the interior domain $0.8 > z > 0.2$. This is a necessary condition for the aforementioned positive feedback. The positive feedback requires the horizontal and vertical motions (u and w) in the cross-band vertical plane be accelerated by the Coriolis force associated with v and buoyancy b, respectively, which means that $\langle uv \rangle$ and $\langle wb \rangle Ri$ should be positive and so should their sum C_2.

In general, a positive feedback requires the sum of energy conversion terms to be positive in each of the three equations in (2.1). For the symmetric mode, v is generated solely by $J(\psi, M)$ and thus is positively correlated with $J(\psi, M)$. This explains why $C_v = \langle vJ(\psi, M) \rangle$ is positive over the entire depth (except for the two non-slip boundaries where v vanishes), as shown in figure 3(*b*). Similarly, $C_b = \langle bJ(\psi, B) \rangle$ is positive over the entire depth (except for the two non-slip boundaries where b vanishes), as shown in figure 3(*b*). However, as shown in figure 3(*a*), C_2 is positive only in the interior domain ($0.8 > z > 0.2$), so the positive feedback is confined within the interior domain. As explained above, this positive feedback requires $\langle uv \rangle$ and $\langle wb \rangle Ri$ to be positive in the energy conversions. This type of energy conversion is called symmetric.

The energy conversions C_v and C_b reach their maxima near the two boundaries (figure 3*b*, *c*). These maxima are associated with the *v*-cores in figure 2(*b*) and *b*-cores in figure 2(*c*), respectively. As explained in § 3.1, these cores are generated in association with the local deceleration of the cross-band flow near the boundaries. This gives a negative feedback to the cross-band circulation near the boundaries where C_2 becomes negative as shown in figure 3(*a*).

The energy dissipation terms D_2, D_v and D_b are virtually zero in the interior domain but jump to negative values at the boundaries (figure 3*a*–*c*). When D_2 is combined with C_2 on the right-hand side of (2.2*a*), the negative D_2 spikes offset the C_2 jumps at the two boundaries. However, when D_v is combined with C_v on the right-hand side of (2.2*b*), the negative D_v spikes enhance the decrease of $C_v + D_v$ at the boundaries. A similar situation is seen when D_b is combined with C_b on the right-hand side of (2.2*c*). The enhanced boundary decreases in $C_v + D_v$ and $C_b + D_b$ demonstrate the negative impact of the non-slip boundary conditions on the energy production. When the non-slip boundary conditions are replaced by the free-slip ones or the Ekman number becomes zero, all the boundary spikes diminish in the energy dissipation profiles and all the near-boundary decreases in the energy conversion profiles disappear, but the interior profiles remain almost intact (not shown).

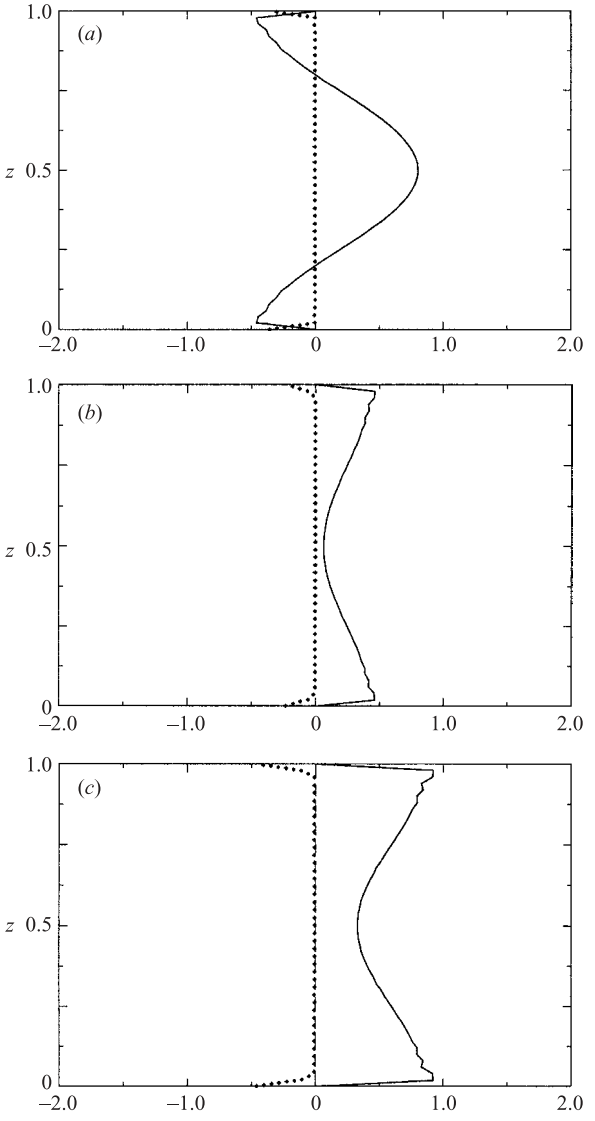

FIGURE 3. Vertical profiles of (*a*) C_2 (solid) and D_2 (dotted), (*b*) C_v (solid) and D_v (dotted), and (*c*) C_b (solid), $\langle vb \rangle \sin\alpha/Ri$ (dashed) and D_b (dotted) for the non-slip symmetric mode in figure 2. Note that $\langle vb \rangle \sin\alpha/Ri = 0$ for the symmetric modes ($\alpha = 0$). Here, C_2, C_v and C_b are the energy conversions defined in (2.3), while D_2, D_v and D_b are the dissipation terms defined in (2.5). All the terms are normalized by the volume-averaged total energy $\{E\}$ defined in (2.7).

3.3. *Effects of increased diffusivity*

When the Ekman number is increased to 0.01, the boundary spikes in the energy dissipation profiles and the sharp edges in the energy conversion profiles in figure 3 are all diffused into deep boundary layers (not shown). In this case, the boundary-layer depth is increased by an order of magnitude, and the energy dissipation terms drop to relatively large negative values near and at the boundaries. The interior profiles remain roughly the same as those in figure 3 but C_b is decreased significantly. The slanted downdraught is still between the M-surface and B-surface in the interior

domain and thus is accelerated by the same type of positive feedback as explained in § 3.1, except that the positive feedback is weakened due to the increased diffusivity.

Unlike the above non-slip mode, the free-slip symmetric mode at $(l, \alpha) = (1, 0)$ becomes a decaying mode as Ek increases to 0.01. In this case, the diffused v-cores and b-cores are shifted along the two free-slip boundaries and become negatively correlated with their respective generation terms $J(\psi, M)$ and $J(\psi, B)$. Because of these structure changes (not shown), the positive feedback is dramatically weakened and confined in a shallow layer (between $0.65 > z > 0.35$) as indicated by the energy conversion profiles (not shown). The total energy generation is thus insufficient to overcome the total energy dissipation (although the energy dissipation is zero at the free-slip boundaries), so the growth rate becomes negative.

4. Warm-side tilted nearly symmetric modes

4.1. *Mode structures and instability mechanism*

Figure 4 shows the structures of ψ, v, b and G for the non-slip mode at $(l, \alpha) = (1, -12^\circ)$ with $Ek = 0.0001$ and $Ri = 0.5$. Since the band is tilted to the warm side of the basic shear ($\alpha < 0$), the cross-band component of the basic flow, given by $(z - 0.5)\sin\alpha$, is no longer zero. The near-boundary basic-flow directions are sketched by the two hollow arrows in figure 4(a). As the cross-band circulation is stretched by the basic shear, it becomes more slanted than those in figure 2(a). The M-surface and B-surface (intersections in the cross-band vertical plane) in figure 4(a) are slightly closer to each other than in figure 2, but the slanted downdraught is still between the two surfaces and thus is accelerated by mainly the same positive feedback as explained for the symmetric mode in § 3.1. This positive feedback is further enhanced by the v-advection of the basic-state buoyancy in the middle levels, because the v-advection term $-v\partial_y B = v\sin\alpha/Ri$ is proportional to $-v$ (for $\alpha < 0$) and v is negatively correlated with b in the middle levels (see figure 4b, c). The slanted updraught is also accelerated by this type of positive feedback and so is the slanted cross-band circulation. The positive feedback is manifested by the negative correlation between ψ and G in the interior domain (figure 4a, d).

The slanted downdraught in figure 4(a) is closer to the M-surface than in figure 2(a). This implies that v is reduced slightly and b is enhanced negatively along the downdraught in the middle levels (compare figures 4b, c and 2b, c). As explained above, b is also enhanced negatively by $-v\partial_y B$ in the middle levels along the downdraught. Since $\partial_z v$ is small and $-Ri\,\partial_x b$ is the dominant part of G in the middle levels, G is enhanced negatively (or positively) on the right (or left side) of the downdraught, as shown by comparing figures 4(d) and 2(d). This means that the enhanced G-field is positively correlated with the vorticity field, so the vorticity generation is increased in the middle levels and the streamlines are tightened toward the circulation centres away from the two boundaries (compare figures 4a and 2a). In this case, the near-boundary cross-band flow becomes relatively weak, so the maxima of $J(\psi, M)$ and $J(\psi, B)$ are reduced and shifted further away from the boundaries. Note that the v-cores are not only generated by $J(\psi, M)$ but also stretched and advected by the basic shear, so the positive v-core (marked by $\otimes$) in figure 4(b) is not only weaker and located further away from the lower boundary but also more slanted and located further rightward than in figure 2(b). As the positive buoyancy perturbation generated by $J(\psi, B)$ is largely offset by $-v\partial_y B$ in the positive v-core area, the b-core (marked by $+$ in figure 4c) is shifted to the upper-left side of the v-core.

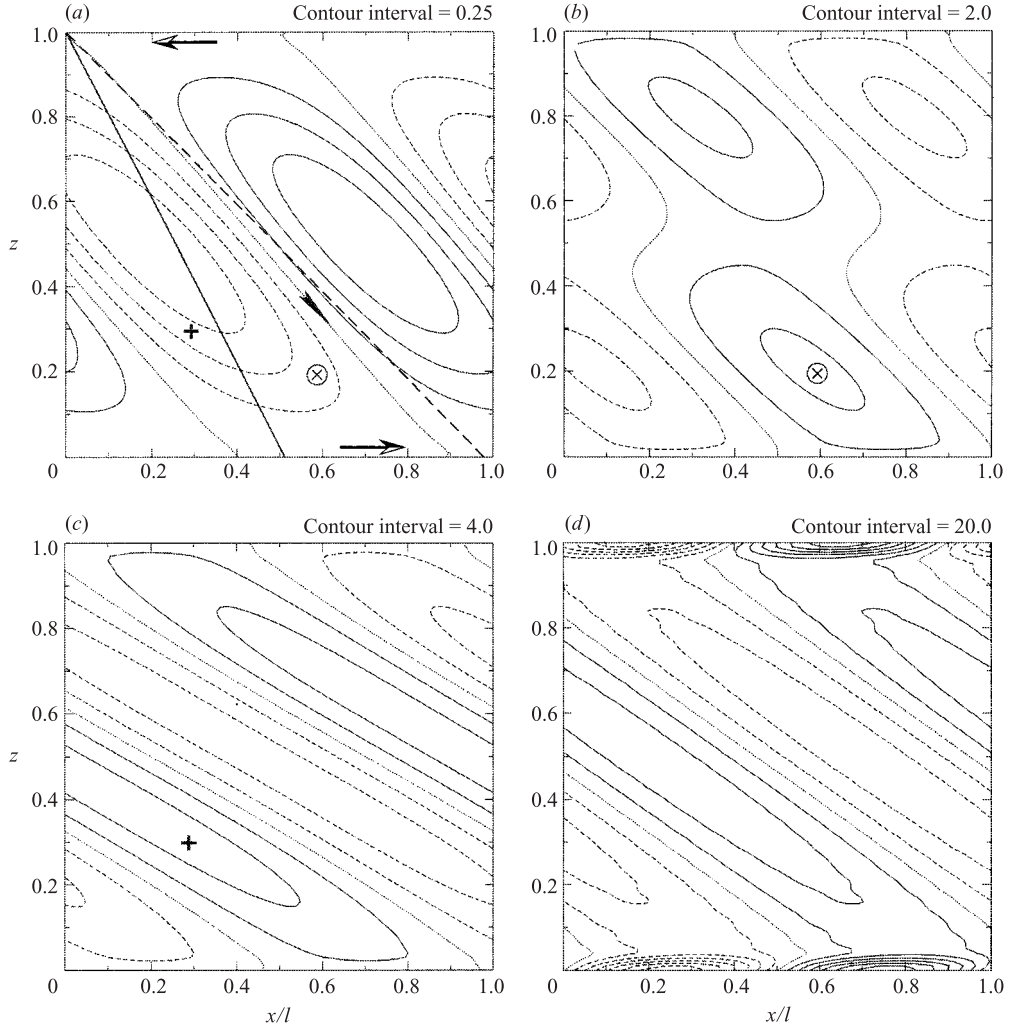

FIGURE 4. As in figure 2 but for $(l, \alpha) = (1, -12°)$. The amplitudes of v, b and G are 5.0, 9.8 and 134.4, respectively. The growth rate is 0.488. The basic-flow shear (projected in the cross-band vertical plane) is sketched by the two horizontal hollow arrows near the lower and upper boundaries.

Because the v-cores in figure 4(b) are weaker and located further away from the boundaries than those in figure 2(b), the shallow G-cores along the boundaries in figure 4(d) are much weaker than those in figure 2(d). When the non-slip boundary conditions are replaced by the free-slip ones or the Ekman number becomes zero, the v-cores and b-cores are shifted onto the boundaries and the shallow G-cores disappear completely (not shown), but the interior fields remain the same as in figure 4.

4.2. *Energy analysis*

For the warm-side tilted mode, C_2 is increased in the interior domain (compare figures 5a and 3a). The increased C_2 is consistent with enhanced vorticity generation, as explained in § 4.1. Also, as the cross-band perturbation flow becomes relatively deep and weak near the boundaries, u, w, v and b are all weakened near the boundaries.

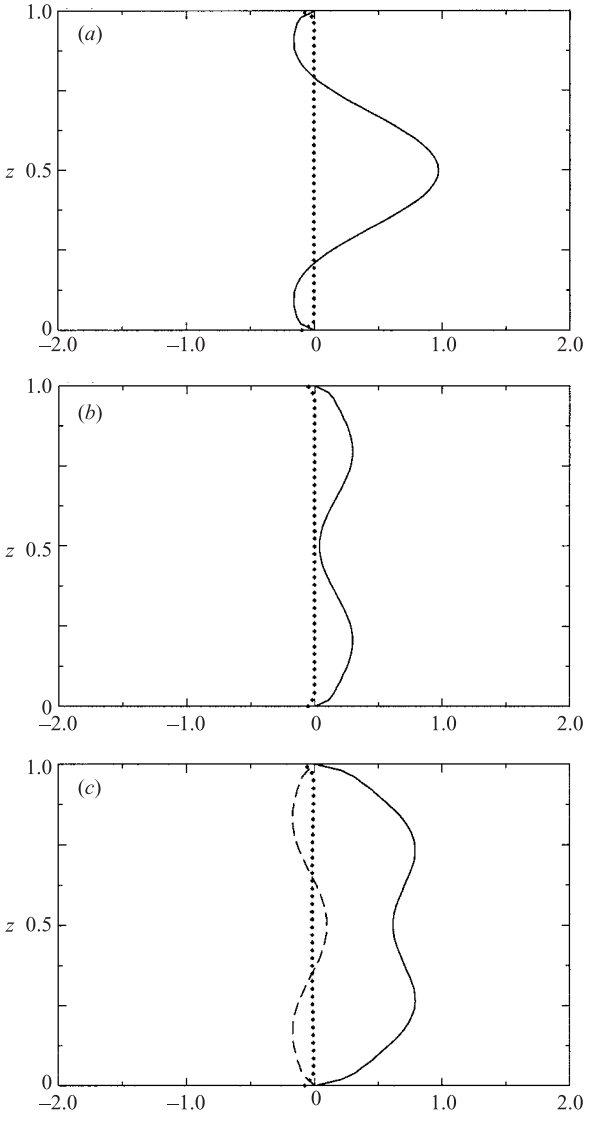

FIGURE 5. As in figure 3 but for $(l, \alpha) = (1, -12^\circ)$.

This explains why the absolute values of C_2, C_v and C_b are all reduced near the boundaries (compare figures 5*a–c* and 3*a–c*).

The dashed profile in figure 5(*c*) shows that the potential energy conversion due to the along-band buoyancy advection (represented by $\langle vb \rangle \sin\alpha$ with $\sin\alpha < 0$) is positive in the middle levels but is negative in the lower and upper levels. This result is consistent with the correlation between v and b, which is negative in the middle levels but positive in the lower and upper levels (figure 4*b*, *c*). The vertical average of this conversion term is negative but very small. Its contribution to the potential energy production can be neglected in comparison with the first term C_b in (2.2*c*) as shown in figure 5(*c*). Note that the total potential energy conversion $C_b + \langle vb \rangle \sin\alpha$ is increased (compare figures 5*c* and 3*c*) and the energy conversion C_2 is also increased in the interior domain (figures 5*a* and 3*a*), so the positive feedback is enhanced. This

explains why the warm-side tilted mode grows faster than the symmetric mode (with $l = 1.0$ and $Ek = 0.0001$).

It is observed (not shown) that $\langle wb \rangle Ri$ is positive over almost the entire depth and maximized at the middle level, so the perturbation buoyancy flux is upward. As shown in figure 5(c), in a relatively shallow middle layer, $\langle vb \rangle \sin\alpha$ is positive and thus $\langle vb \rangle$ is negative, so the perturbation buoyancy flux is toward the negative y-direction to the cold side (since the y-direction is tilted to the warm side of the basic shear). Hence, the perturbation transports warm air to the cold side with rising motion and transports cold air to the warm side with sinking motion, in the middle levels in the along-band vertical plane (y, z). This feature is typical of the baroclinic mode, although here it is exists only in a shallow middle layer. The associated energy conversion requires that both $\langle wb \rangle Ri$ and $\langle vb \rangle \sin\alpha$ be positive, which characterizes the baroclinic-type energy conversion (see § 6.4). While the growth of the warm-side tilted nearly symmetric mode is supported mainly by the symmetric-type energy conversion through the positive feedback explained above, it is also assisted by the baroclinic-type energy conversion in the middle levels.

The energy dissipation profiles (dotted) in figure 5(a–c) show negative spikes at the boundaries, but these spikes are much smaller than those in figure 3(a–c). The smallness of boundary energy dissipation in figure 5 is a direct consequence of the smoothness of the near-boundary structures in figure 4(a–c). The near-boundary smoothness is produced dynamically in association with the baroclinic-type energy conversion, which is negative near the boundaries, so it is an inviscid feature of the warm-side tilted modes. Hence, the warm-side tilted modes are less severely damped by the increased diffusivity than the cold-side tilted modes, especially for the non-slip case (see §§ 4.3 and 5.3). This explains why the global maximum point in the growth rate pattern moves along the negative-α branch as the Ekman number increases (compare figure 1 with figures 3 and 2a of part 1).

When the non-slip boundary conditions are replaced by the free-slip ones or the Ekman number becomes zero, the small boundary spikes diminish in the energy dissipation profiles and the energy conversion profiles are moved slightly away from zero at the boundaries, but the interior profiles remain almost intact (not shown). As the energy dissipation reduces to zero at the free-slip boundaries, the growth rate increases slightly from $\sigma = 0.488$ (for the non-slip mode) to 0.496 (for the free-slip mode).

4.3. *Effects of increased diffusivity*

When the Ekman number increases from 0.0001 to 0.01, the growth rate for the non-slip mode at $(l, \alpha) = (1, -12^\circ)$ decreases from 0.488 to 0.244. In this case, as shown in figure 6(a), C_2 is enhanced in the middle level from the already increased value in figure 5(a) (from that in figure 3a). The energy dissipation D_2 (dotted in figure 6a) is increased negatively, but the sum of C_2 and D_2 is still positive in the interior domain. This implies that the interior dynamics and related instability mechanism remain qualitatively the same, as explained for the nearly inviscid mode in figure 4. As shown in figure 7(a), the slanted downdraught is still between the M-surface and B-surface and thus is accelerated by the same positive feedback mechanism as described for the nearly inviscid mode in § 4.1.

Due to the increased diffusivity, the downdraught is steeper than that in figure 4(a). As the downdraught is tilted vertically away from the M-surface, $J(\psi, M)$ is enhanced along the downdraught. Because of this and the enhanced diffusivity, the positive v-core is shifted to the middle levels and becomes elongated close to the downdraught

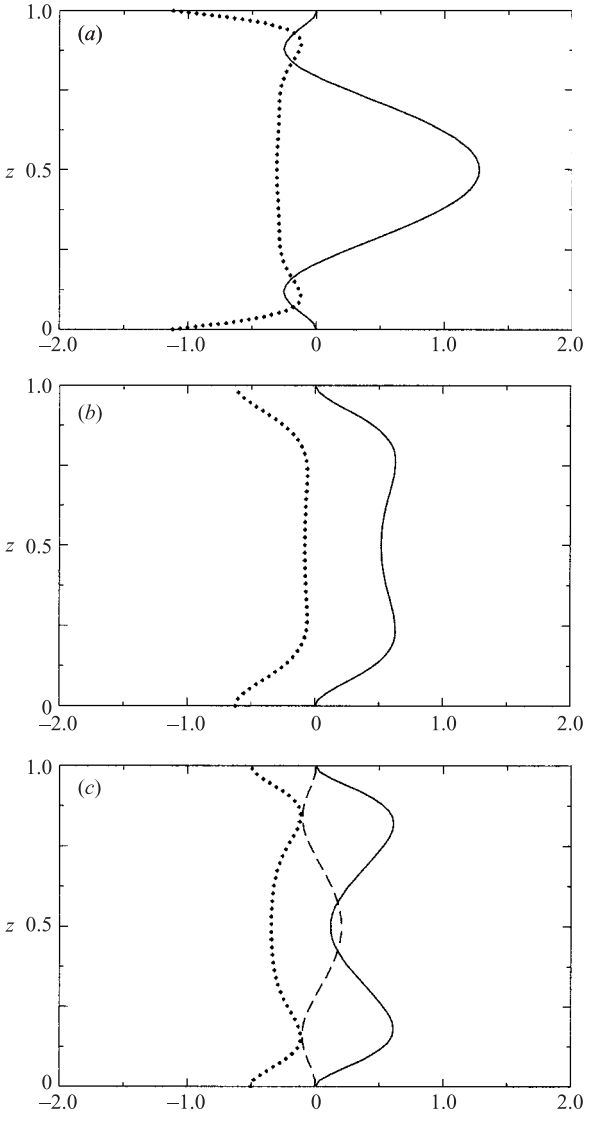

FIGURE 6. As in figure 3 but for $(l, \alpha) = (1, -12^\circ)$ with $Ek = 0.01$.

(figure 7*b*). As the downdraught is tilted vertically toward the B-surface, $J(\psi, B)$ is reduced along the downdraught. The positive b generated by $J(\psi, B)$ is further reduced by $-v\partial_y B$ in the positive v-core area. Thus, although the b-cores are shifted away from the boundaries due to the enhanced diffusivity, they are not connected in the middle levels (figure 7*c*). The G-cores are expanded into relatively deep boundary layers and their amplitude is decreased (from 134.4 in figure 4*d*) to 55.0 in figure 7(*d*). In response to these structure changes, C_v is enhanced (figure 6*b*) while C_b is reduced (figure 6*c*) but $\langle vb \rangle \sin\alpha$ is enhanced over a relatively deep middle layer (compare figure 6*c* and 5*c*) and so is its contribution to the baroclinic-type energy conversion. This enhances the positive feedback against the increased diffusivity.

As Ek increases to 0.01, the free-slip mode at $(l, \alpha) = (1, -12^\circ)$ is still unstable. Its cross-band circulation is similar to the non-slip mode in figure 7(*a*) except that the

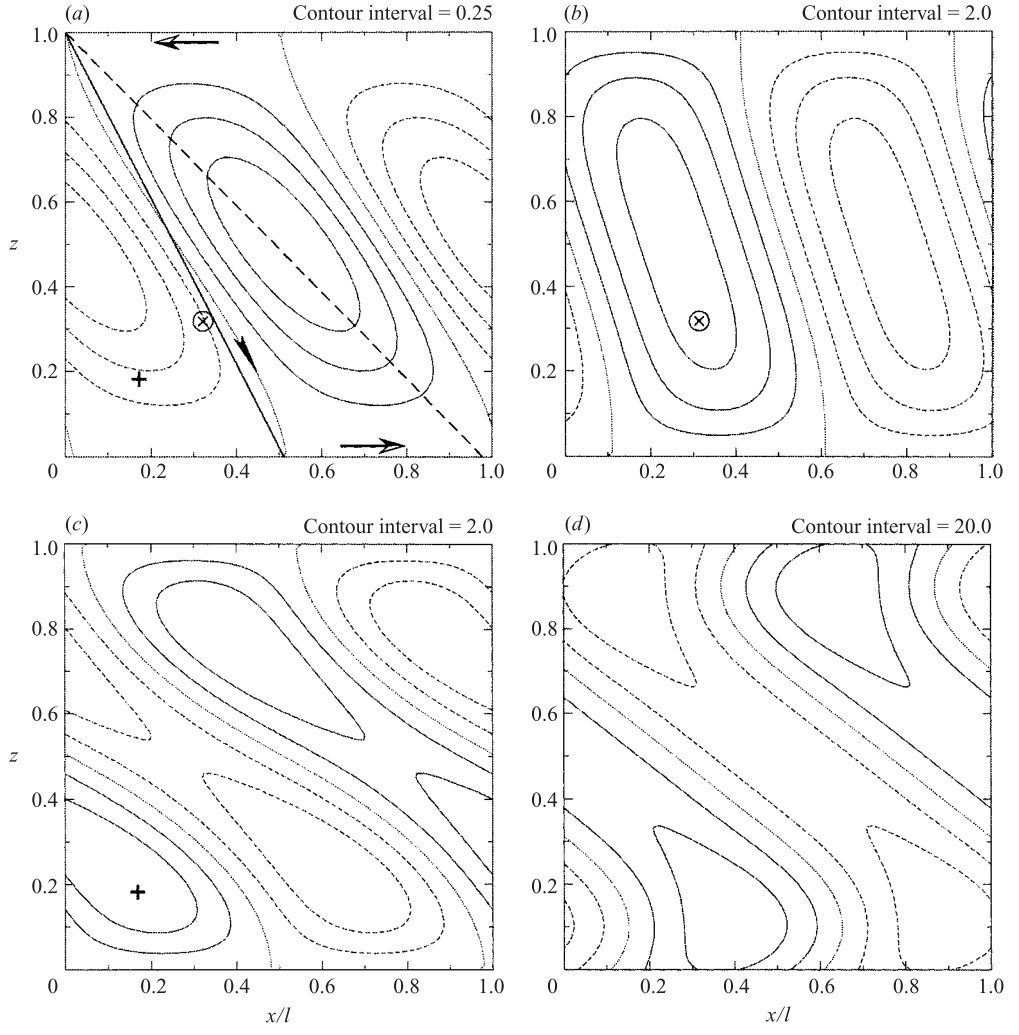

FIGURE 7. As in figure 2 but for $(l, \alpha) = (1, -12^\circ)$ with $Ek = 0.01$. The amplitudes of v, b and G are 7.0, 6.0 and 55.0, respectively. The growth rate is 0.244.

flow is enhanced along the boundaries (not shown). Because of this, the v-cores are extended to the boundaries, the associated v-advection of the basic-state buoyancy further enhances the b-cores along the free-slip boundaries, and the G-cores are also extended to the boundaries (not shown). According to (2.3) and (2.5), the energy conversion terms are no longer zero along the free-slip boundaries but the energy dissipation terms all become to zero along the free-slip boundaries. The interior profiles of these energy terms (not shown) are roughly the same as those for the non-slip case in figure 6. Because the energy dissipation is reduced to zero at the free-slip boundaries, the free-slip growth rate (0.297) is slightly larger than the non-slip one (0.244). Clearly, the growth rates of the warm-side tilted modes are not sensitive to the boundary conditions even when the Ekman number increases to 0.01. This insensitivity can be explained by the aforementioned inviscid feature – the dynamically produced near-boundary smoothness.

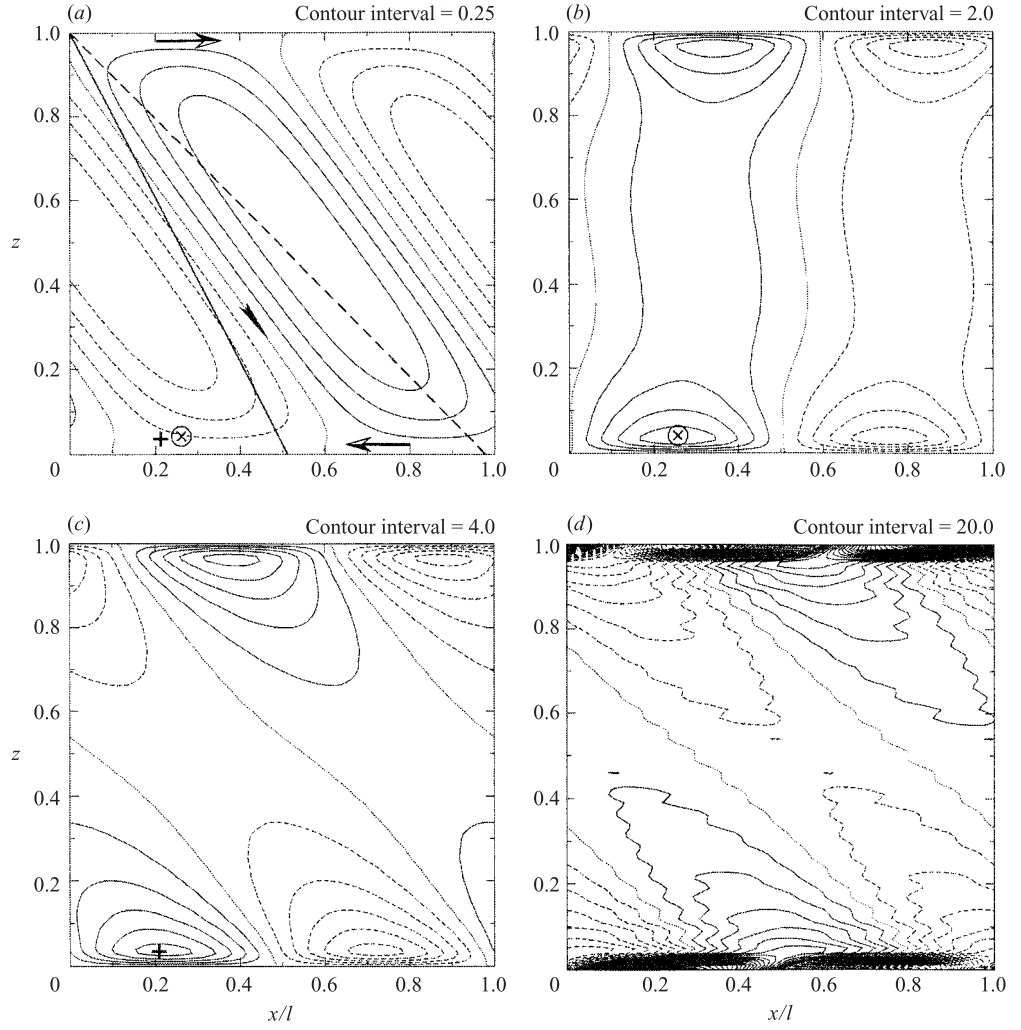

FIGURE 8. As in figure 2 but for $(l, \alpha) = (1, 12^\circ)$. The amplitudes of v, b and G are 10.1, 25.0 and 156.9, respectively. The growth rate is 0.487.

5. Cold-side tilted nearly symmetric modes

5.1. *Mode structures and instability mechanism*

Figure 8 shows the structures of ψ, v, b and G for the non-slip mode at $(l, \alpha) = (1, 12^\circ)$ with $Ek = 0.0001$ and $Ri = 0.5$. As indicated by the two hollow arrows near the two boundaries in figure 8(a), the basic flow projected in the cross-band vertical plane is in the opposite direction to that in figure 4(a) and thus the slanted circulation is steeper than in figure 2(a). The slanted downdraught is still between the M-surface and B-surface and thus is accelerated mainly by the same type of positive feedback as described for the symmetric mode in § 3.1. The overall positive feedback is indicated by the negative correlation between G and ψ in the interior domain (figure 8a, d).

As shown in figure 8(b, c) (compare figure 2b, c), the v-cores and b-cores are intensified and shifted toward the boundaries, and the v-cores are also shifted horizontally following the basic-flow shear. These changes are opposite to those

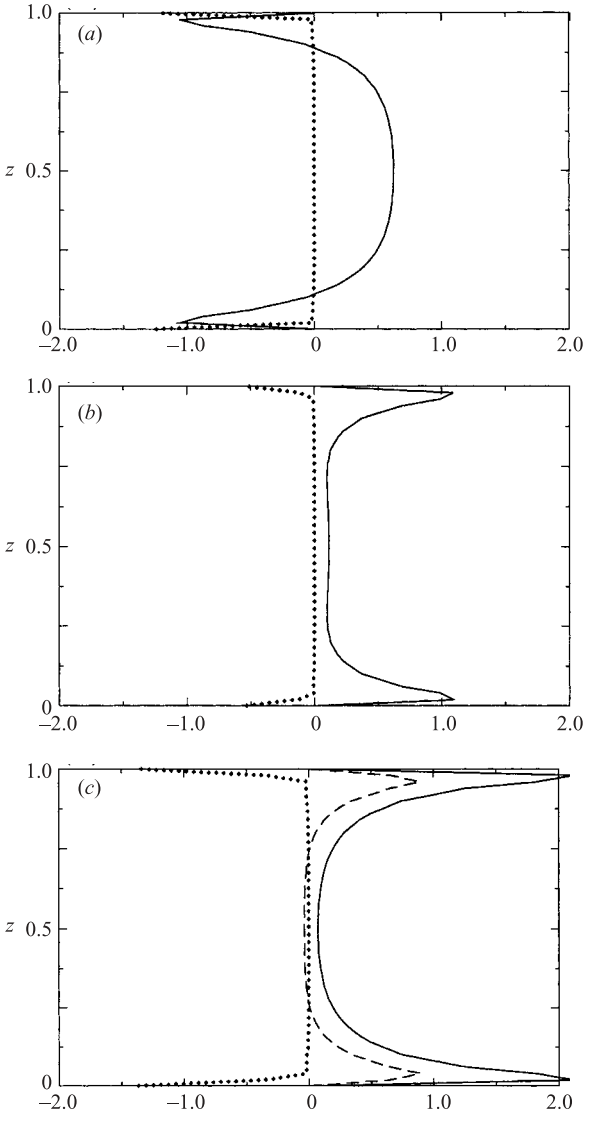

FIGURE 9. As in figure 3 but for $(l, \alpha) = (1, 12°)$.

for the warm-side tilted mode in figure 4(b,c). The associated changes in the G-field (compare figure 8d and 2d) are also opposite to those for the warm-side tilted mode (compare figure 4d and 2d). These changes are related to the increased slope of the slanted circulation (figure 8a) and their relationship can be analysed in the same way, but for opposite case, as for the warm-side tilted mode in § 4.1. When the non-slip boundary conditions are replaced by the free-slip ones or the Ekman number becomes zero, the v-cores and b-cores are shifted onto the boundaries, the very shallow near-boundary G-cores diminish, but the interior fields remain almost exactly the same as in figure 8.

5.2. *Energy analysis*

Associated with the mode structures in figure 8, the C_2 profile drops sharply to large negative values (figure 9a) and the profiles of C_v, C_b and $\langle vb \rangle \sin\alpha$ increase

rapidly to large positive values near the boundaries (figure 9*b*, *c*). These features are opposite to those for the warm-side tilted mode in figure 5 and thus can be explained similarly but in the opposite way. Note that $C_b + \langle vb \rangle \sin\alpha$ is increased dramatically near the boundaries (compare figures 9*c* and 3*c*) and the positive-C_2 layer is expanded toward the boundaries (compare figures 9*a* and 3*a*), so the positive feedback occurs in a relatively deep interior layer. As both $\langle wb \rangle Ri$ (not shown) and $\langle vb \rangle \sin\alpha$ are increased sharply near the boundaries, the baroclinic-type energy conversion is enhanced dramatically near the boundaries. Assisted by this enhanced baroclinic-type energy conversion, the cold-side tilted mode grows faster than the symmetric mode (with $l = 1.0$ and $Ek = 0.0001$).

At the two boundaries, the negative spikes in the energy dissipation profiles (dotted) in figure 9(*a*–*c*) are much larger than those in figure 3(*a*–*c*), and the situation is opposite to that in figure 5. These negative spikes are caused by the non-slip boundary conditions. When the boundary conditions are replaced by the free-slip ones or the Ekman number becomes zero, all the negative spikes diminish in the energy dissipation profiles and all the near-boundary spikes in the energy conversion profiles are extended onto the boundaries, but the interior profiles remain almost intact (not shown). As the energy dissipation is reduced to zero at the free-slip boundaries, the baroclinic-type energy conversion is enhanced near and at the boundaries. Hence, the free-slip growth rate (0.496) is slightly larger than the non-slip one (0.487).

5.3. *Effects of increased diffusivity*

When the Ekman number increases to 0.01, the non-slip mode at $(l, \alpha) = (1, 12^\circ)$ becomes a decaying mode. The free-slip mode at $(l, \alpha) = (1, 12^\circ)$ is still unstable but the growth rate decreases to 0.166. Note that the near-boundary sharpness seen in §§ 5.1 and 5.2 for the cold-side tilted modes is an inviscid feature. This feature is produced similarly but in an opposite way to the near-boundary smoothness for the warm-side tilted modes. It is this feature that causes the non-slip and free-slip modes at $(l, \alpha) = (1, 12^\circ)$ to respond very differently to the increase of diffusivity. Because of this feature, the non-slip mode is much more severely damped by the near-boundary energy dissipation with the increased diffusivity ($Ek = 0.01$) than the free-slip mode. This explains why the positive-α branch of the growth rate pattern drops below zero for the non-slip case but not for the free-slip case as the Ekman number increases to 0.01 (see figures 1*a* and 2*a* of part 1).

6. Nearly baroclinic modes versus baroclinic modes

6.1. *Mode structures and instability mechanism for the warm-side tilted nearly baroclinic mode*

Figure 10 shows the structure of ψ, v, b and G for the non-slip nearly baroclinic mode at $(l, \alpha) = (3.12, -47^\circ)$ with $Ek = 0.0001$ and $Ri = 1.0$. This mode is tilted to the negative side (by -47°) of the symmetric axis in the parameter space or, equivalently, to the warm side of the basic shear in physical space (with α defined within $\pm 90^\circ$ as in (2.1) of part 1). We will call it a warm-side tilted nearly baroclinic mode. The basic shear projected in the cross-band vertical plane is shown by the hollow arrows in figure 10(*a*), similar to that in figure 4(*a*), but the M-surface becomes steeper than the B-surface in the cross-band vertical plane. The slanted downdraught (along the central streamline marked by the arrow) is slightly steeper than the M-surface and much steeper than the B-surface in the cross-band vertical plane. Thus, according to the simple rules stated in § 2.1, $J(\psi, M)$ is slightly positive and so is its generated v

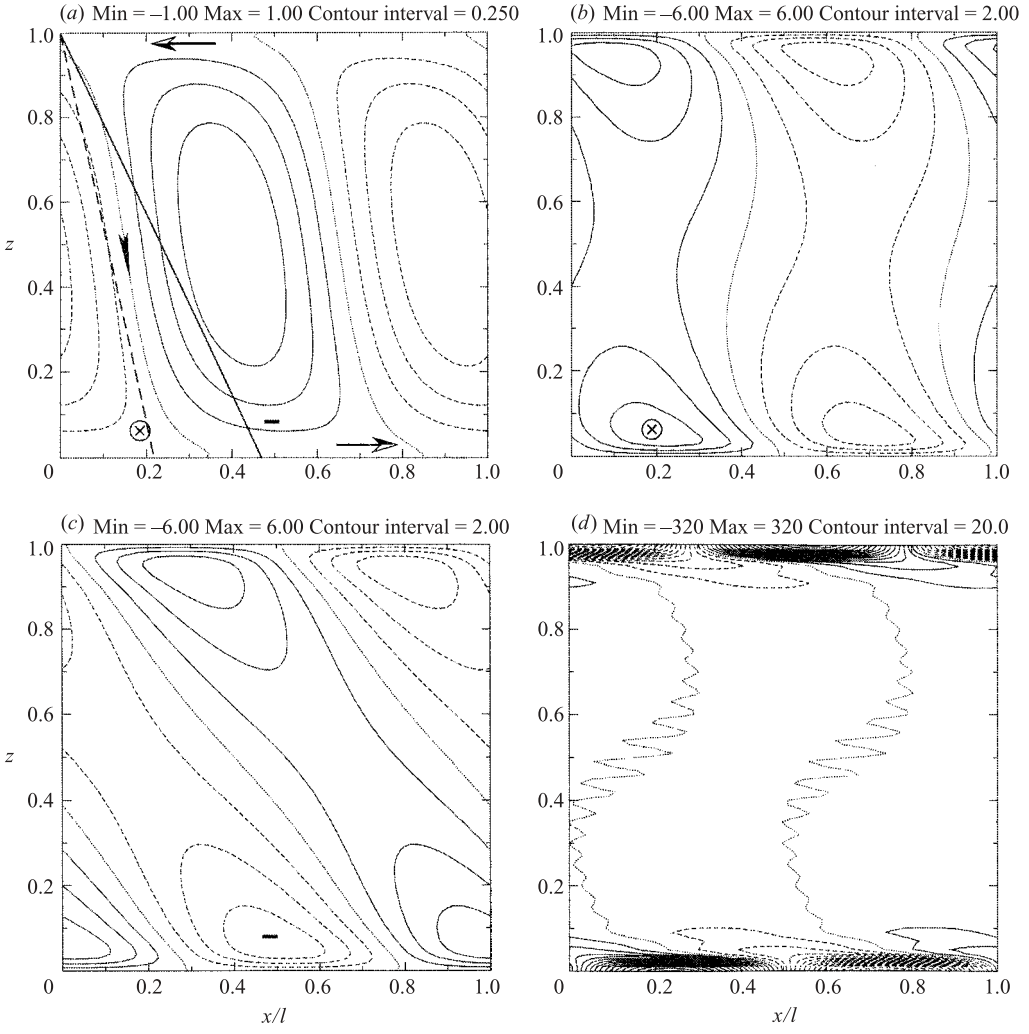

FIGURE 10. As in figure 2 but for $(l, \alpha) = (3.12, -47^\circ)$ with $Ri = 1.0$. The amplitudes of v, b and G are 7.3, 7.7 and 327.4, respectively. The growth rate is 0.172. The negative b-core near the lower boundary is marked by the minus signs in (a) and (c).

along the downdraught (figure 10b). Along the downdraught, $J(\psi, B)$ is positive but the combined generation, $J(\psi, B) - v\partial_y B$, is negative in the middle levels and so is its generated b (figure 10c). Thus, the slanted downdraught is accelerated by the vector force composed of the rightward Coriolis force associated with the positive v and by the downward buoyancy associated with the negative b. This positive feedback depends on the v-advection in (2.1c), which is different from that for the symmetric and nearly symmetric modes.

Because the slanted downdraught is only slightly steeper than the M-surface, $J(\psi, M)$ does not reach the maximum until the downdraught splits and the flow turns into the leftward branch near the lower boundary. As soon as the positive v-core is generated by $J(\psi, M)$, it is advected by the basic flow away from the maximum of $J(\psi, M)$ to the downdraught exit area (marked by $\otimes$ in figure 10a, b). The v-advection term $-v\partial_y B$ is negative in the positive v-core area. Its generated

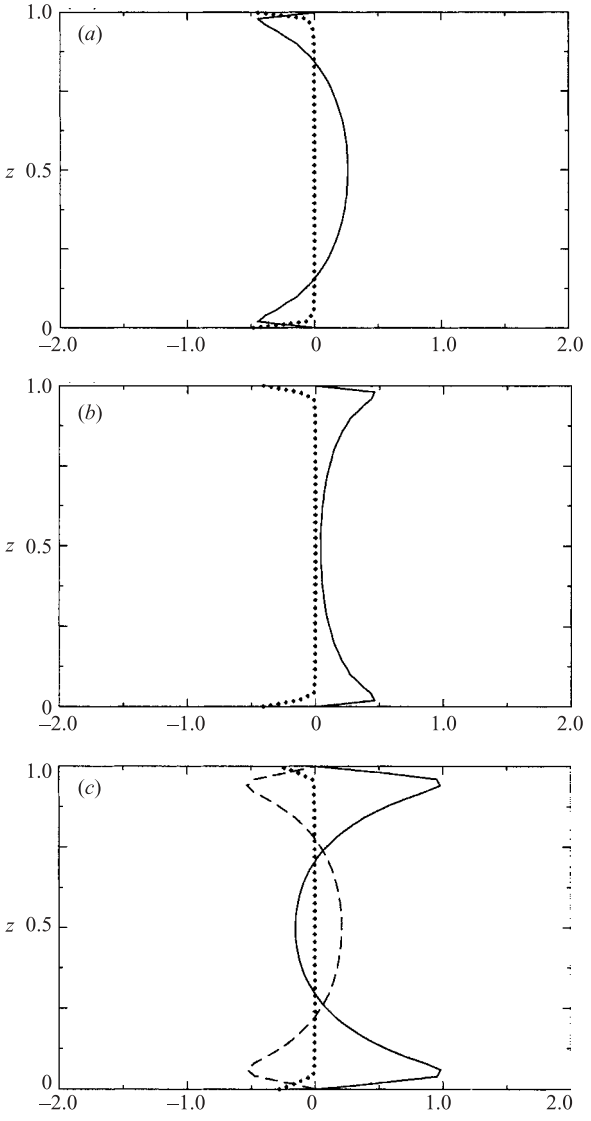

FIGURE 11. As in figure 3 but for $(l, \alpha) = (3.12, -47^\circ)$ with $Ri = 1.0$.

negative b-core is advected rightward by the basic flow and enhanced by $J(\psi, B)$ along the rightward branch of the cross-band flow. Thus, the negative b-core is near the lower boundary between the two stagnation points (marked by the minus signs in figure 10a, c). The shallow G-cores (figure 10d) are associated with the very strong vertical gradient of v near the non-slip boundaries. When the non-slip boundary conditions are replaced by the free-slip ones or the Ekman number becomes zero, the v-core and b-core centres are shifted to the boundaries and the shallow G-cores largely diminish but the interior fields remain almost the same.

6.2. *Energy analysis for the warm-side tilted nearly baroclinic mode*

As shown in figure 11(a), C_2 is positive in the interior domain, and this is consistent with the negative correlation between ψ and G in the interior domain (figure 10a, d).

The C_v profile (figure 11*b*) and C_b profile (figure 11*c*) reach their maxima near the two boundaries. Note that $C_v = \langle J(\psi, M)v\rangle$ and $C_b = \langle J(\psi, B)b\rangle$; these maxima are associated with the v-cores and b-cores and their positive correlations with $J(\psi, M)$ and $J(\psi, B)$, respectively. These cores are generated in association with the local deceleration of the cross-band flow near the boundaries. The local deceleration implies a negative feedback to the cross-band circulation near the boundaries, as reflected by the negative peaks of C_2 near the boundaries in figure 11(*a*).

As shown in figure 11(*b*), C_v is small but still positive at the middle level. This is consistent with the reduced $J(\psi, M)$ in the middle levels where the downdraught is slightly steeper than the M-surface (figure 10*a*). As shown in figure 11(*c*), C_b is negative at the middle level but $C_b + \langle vb\rangle \sin\alpha$ is positive. Thus, as mentioned earlier, the b-field is mainly generated by $-v\partial_y B$ in the middle levels. Since $\langle wb\rangle Ri$ is positive over the entire depth (not shown) and $\langle vb\rangle \sin\alpha$ is positive in the middle levels (figure 11*c*), the growth of the warm-side tilted nearly baroclinic mode is supported by the baroclinic-type energy conversion in the middle levels.

The boundary spikes in the energy dissipation profiles (dotted in figure 11) are similar to those in figure 3. The negative D_2 spikes offset the C_2 jumps at the two boundaries, so $C_2 + D_2$ on the right-hand side of (2.2*a*) is the same as C_2 except that the boundary jumps are eliminated. The negative D_v spikes, however, enhance the drops of $C_v + D_v$ at the boundaries. The negative D_b spikes also enhance the decrease of $C_b + \langle vb\rangle \sin\alpha + D_b$ at the boundaries. The enhanced boundary drops on the right-hand sides of (2.2*b*) and (2.2*c*) demonstrate the negative impact of the non-slip boundary conditions on the energy production. When the non-slip boundary conditions are replaced by the free-slip ones or the Ekman number becomes zero, all the boundary spikes diminish in the energy dissipation profiles and all the near-boundary decreases in the energy conversion profiles disappear, but the interior profiles remain almost intact (not shown).

6.3. *Effects of increased diffusivity on the warm-side tilted nearly baroclinic modes*

When the Ekman number increases from 0.0001 to 0.01, the boundary spikes in figure 11 are diffused into deep boundary layers as shown in figure 12. The total potential energy conversion $C_b + \langle vb\rangle \sin\alpha$ is still positive over the entire depth (figure 12*c*), but the depth of the positive-C_2 layer is reduced (compare figures 12*a* and 11*a*) and C_v is nearly zero at the middle level (figure 12*b*). Hence, the positive feedback is weakened by the increased diffusivity. In response to the increased diffusivity, the positive v-cores are expanded to the middle levels in the vicinity of the downdraught, the negative b-cores are connected into a single core at the middle level, and the G-cores are expanded into relatively deep boundary layers but G-field is still negatively correlated with the ψ-field. These mode structure changes (not shown) are consistent with the energy analysis in figure 12, and their implied positive feedback remains qualitatively the same, as discussed in § 6.1 for the nearly inviscid mode.

6.4. *Comparisons with purely baroclinic modes*

The nearly baroclinic mode discussed in figure 12 is at the global maximum point $(l, \alpha) = (3.12, -47^\circ)$ in the growth rate pattern (figure 2*c* of part 1). When the parameter point moves from this global maximum point to the conditional maximum point (3.12, -90°), the growth rate decreases from 0.106 to 0.084. In this case, the energy conversion terms C_2, C_v and $C_b + \langle vb\rangle \sin\alpha$ are reduced slightly in the middle levels. These structure changes (not shown) indicate that the positive feedback is

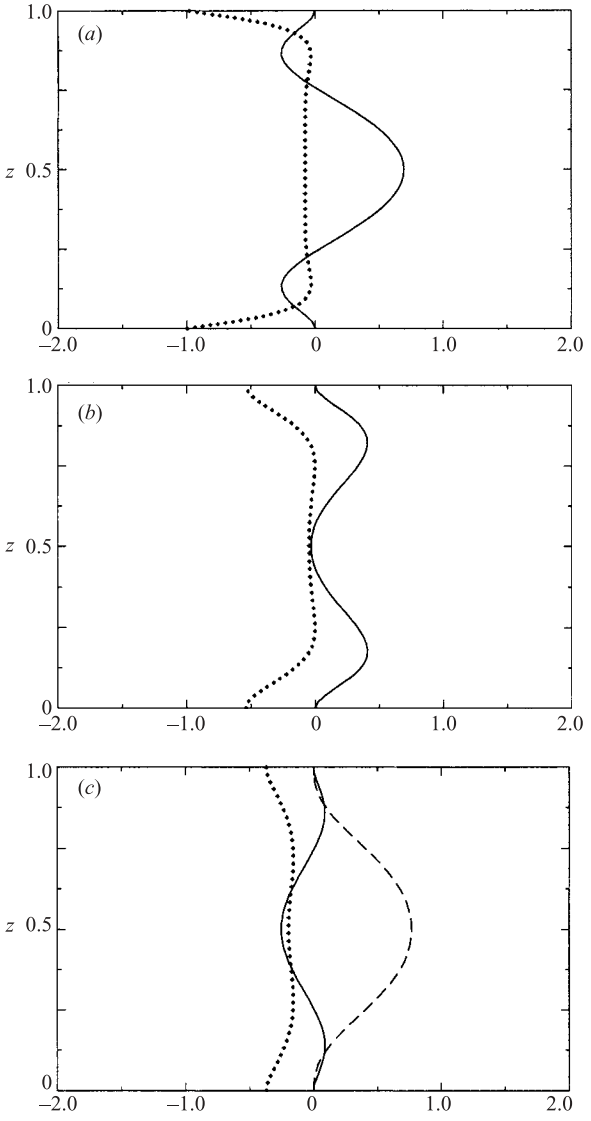

FIGURE 12. As in figure 3 but for $(l, \alpha) = (3.12, -47°)$ with $Ri = 1.0$ and $Ek = 0.01$.

weakened slightly, so the baroclinic mode grows slower than the nearly baroclinic mode.

For the baroclinic mode, the y-direction is perpendicular to the basic shear and points southward to the warm side (with $\alpha = -90°$), so the basic-state buoyancy gradient is along the y-direction and is given by $-\sin\alpha/Ri = 1/Ri$. In this case, $\langle wb \rangle = -C_b/Ri$ is positive and $\langle vb \rangle = -\langle vb \rangle \sin\alpha$ is negative (not shown), so the perturbation buoyancy flux is upward and northward in the along-band vertical plane. This means that the perturbation transports warm air northward with rising motion and transports cold air southward with sinking motion. This feature is essential for the growth of the classic baroclinic waves (§ 9.3 of Holton 1979). It implies that the perturbation parcel trajectories must be less steep than the basic-state potential

temperature surfaces in (y, z) for an unstable baroclinic mode. The associated energy conversion is characterized by the positiveness of both $\langle wb\rangle Ri$ and $\langle vb\rangle \sin\alpha$. This type of energy conversion is called the baroclinic type, as mentioned in § 4.2.

6.5. *Comparisons with cold-side tilted nearly baroclinic modes*

When the parameter point moves from $(l, \alpha) = (3.12, -47^\circ)$ to $(3.12, 47^\circ)$ in the growth rate pattern (figure 2*c* of part 1), the growth rate decreases from 0.106 to 0.013. In this case, the amplitudes of C_2, C_v and $C_b + \langle vb\rangle \sin\alpha$ are reduced by nearly 50% from those in figure 12(*a*–*c*), while the energy dissipation term D_b increases negatively to nearly -1.0 at the boundaries. These structure changes (not shown) indicate that the positive feedback becomes much weaker, hence the growth rate (0.013) is much smaller than that (0.106) of the warm-side tilted mode at $(l, \alpha) = (3.12, -47^\circ)$.

When Ek decreases to 0.0001, the growth rate of the cold-side tilted baroclinic mode increases to the same value (0.172) as that of the warm-side tilted nearly baroclinic mode in figure 10. As shown in figure 13, the energy conversion profiles of C_2, C_v and $C_b + \langle vb\rangle \sin\alpha$ are similar to those in figure 11, although the partitioned profiles of C_b and $\langle vb\rangle \sin\alpha$ are very different from those in figure 11(*c*). This overall similarity explains why the two tilted modes have almost the same growth rate. The negative spikes at the boundaries in the energy dissipation profiles in figure 13 are much larger than those in figure 11. The enhanced negative spikes are associated with the enhanced v-cores and b-cores near the boundaries (not shown). These structure differences explain why the growth rate (0.013) of the cold-side tilted nearly baroclinic mode becomes much smaller than that (0.106) of the warm-side tilted mode as the Ekman number increases to 0.01.

7. Volume-averaged energy

7.1. *Energy for the symmetric and nearly symmetric modes*

As explained in § 3.2, the symmetric-type energy conversion requires that both $\{\langle uv\rangle\}$ and $\{\langle wb\rangle\}Ri$ be positive. Under this condition, the first energy conversion terms in (2.6*b*) and (2.6*c*) are negative. Since $\sin\alpha = 0$ for the symmetric modes, the third energy conversion terms vanish in (2.6*b*) and (2.6*c*). Hence, the second energy conversion terms in (2.6*b*) and (2.6*c*) should be not only positive but also sufficiently large to ensure that the sums of the conversion terms be positive to support the growth of the symmetric mode. The signs of the energy conversion terms in (2.6) are thus all determined, as verified by the computed energy conversions for the non-slip symmetric modes in the vicinity of the conditional maximum. An example is shown by the values at $\alpha = 0$ in figure 14(*a*) for the non-slip mode at $(l, \alpha) = (1.0, 0)$. The parameter point for this mode is close to the conditional maximum point at $l = 0.93$ on the symmetric axis (see the growth rate pattern in figure 2*a* of part 1). When the parameter point moves along the symmetric axis in the vicinity of the conditional maximum, the energy terms in (2.6) do not change their signs (not shown). The energy conversions for the symmetric modes in the vicinity of the conditional maximum are shown by the solid boxes of the diagram in figure 15. As the parameter point moves away from the symmetric point at $\alpha = 0$ into the range $-36^\circ \leqslant \alpha < 0^\circ$ of the main growth rate pattern for the non-slip modes (figure 2*a* of part 1), all the energy terms in (2.6) do not change their signs although $-\{\langle uw\rangle\}\sin\alpha$ and $\{\langle vb\rangle\}\sin\alpha$ are no longer zero (figure 14*a*). The energy conversions for the nearly symmetric modes in the vicinity of the global maximum are summarized in figure 15.

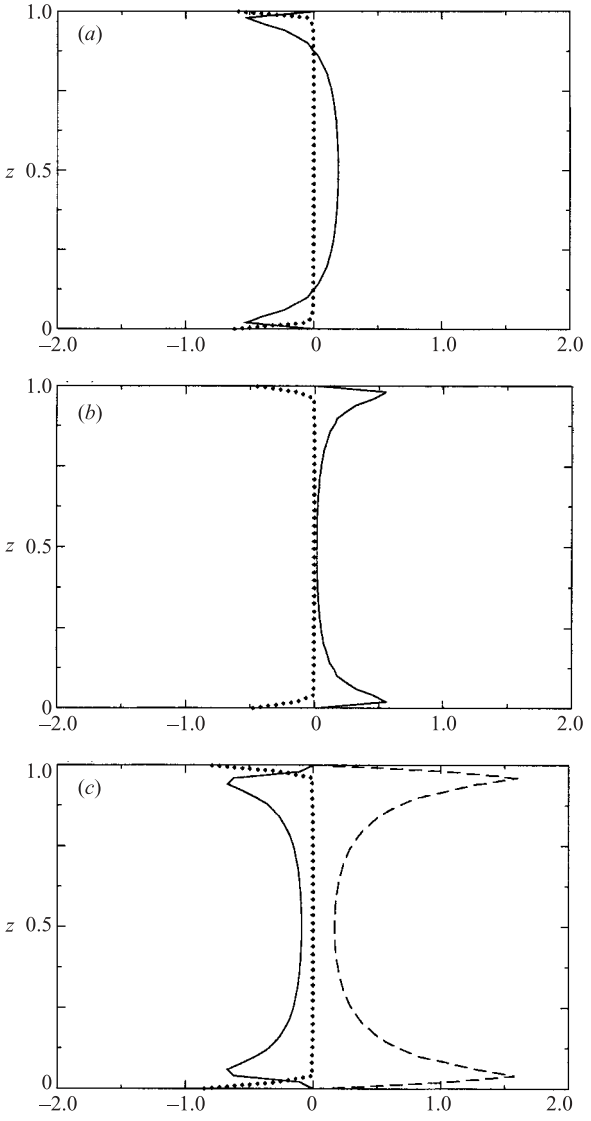

FIGURE 13. As in figure 3 but for $(l, \alpha) = (3.12, 47°)$ with $Ri = 1.0$.

The free-slip nearly symmetric modes cover two ranges: $-23° \leqslant \alpha < -1°$ and $7° \leqslant \alpha < 28°$ along $l = 1.0$ in the growth rate pattern (figure 1*a* of part 1). As shown in figure 14(*b*), for the warm-side tilted free-slip modes ($-23° \leqslant \alpha < -1°$), all the energy conversion terms except for $\{\langle vb \rangle\} \sin\alpha$ have the same signs as those in figure 14(*a*). Although $\{\langle vb \rangle\} \sin\alpha$ becomes negative, the total potential energy conversion $\{C_{Bb}\} = \{\langle vb \rangle\} \sin\alpha - \{\langle ub \rangle\} \cos\alpha$ is positive, so the energy conversion diagram is the same as in figure 15. For the cold-side tilted nearly symmetric modes ($7° \leqslant \alpha < 28°$ in figure 14*b*), most of the energy conversion terms have the same signs as those in figure 14(*a*) except that $\{C_{U2}\} = -\{\langle uw \rangle\} \sin\alpha$ and $\{\langle uv \rangle\}$ change signs. Thus, the directions of the latter two conversions are opposite to those in figure 15.

As shown by the energy dissipation curves in figure 14(*a*, *b*), the total energy dissipation is stronger for the warm-side tilted non-slip modes ($-36° \leqslant \alpha < 0°$) than

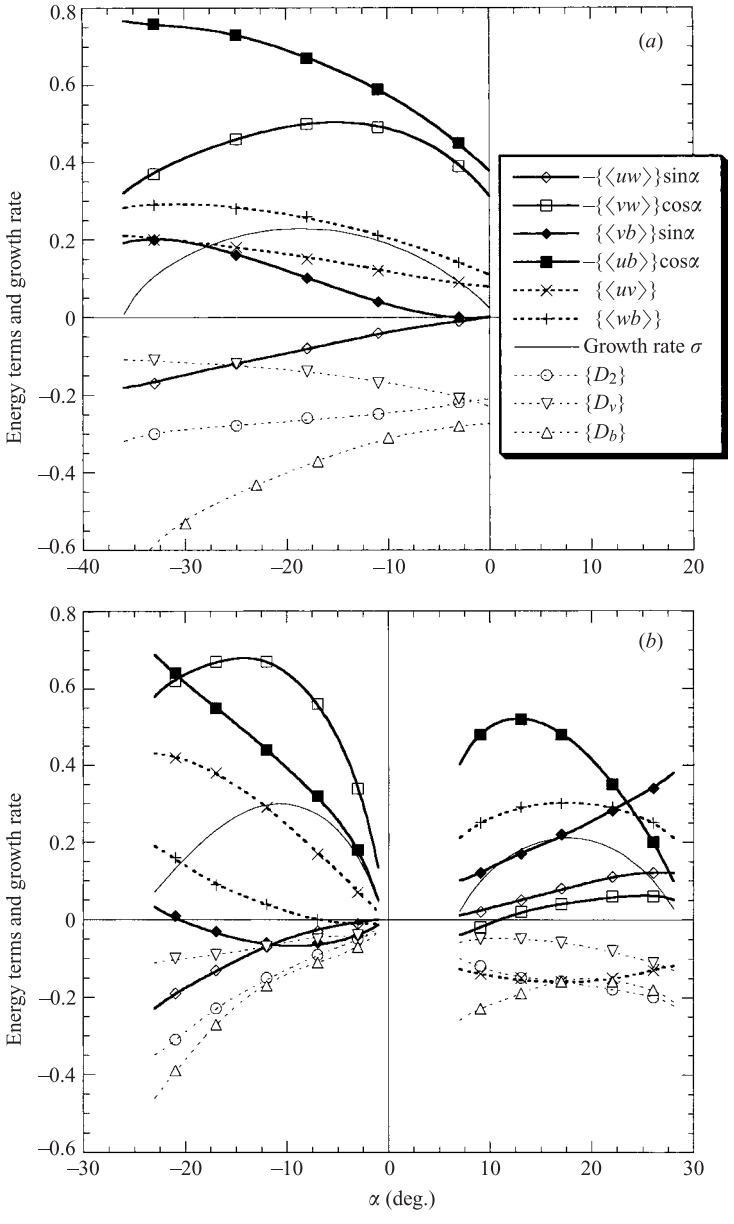

FIGURE 14. Volume-averaged energy terms in (2.6) plotted as functions of α (*a*) for the non-slip nearly symmetric modes in the range ($-36^\circ \leqslant \alpha < 0^\circ$) of the main growth rate pattern ($\sigma \geqslant 0$ and $\omega = 0$) along $l = 1.0$ in figure 2(*a*) of part 1, and (*b*) for the free-slip nearly symmetric modes in the ranges ($-23^\circ \leqslant \alpha < -1^\circ$ and $7^\circ \leqslant \alpha < 28^\circ$) of the main growth rate pattern along $l = 1.0$ in figure 1(*a*) of part 1. The external parameter values are $Ri = 0.5$, $Ek = 0.01$, $Pr = 1.0$ and $r^2 = 0.02$.

that for the warm-side tilted free-slip modes ($7^\circ \leqslant \alpha < 28^\circ$), while the latter is about the same as that for the cold-side tilted free-slip modes ($-23^\circ \leqslant \alpha < -1^\circ$). The cold-side tilted non-slip modes are all decaying modes due to the dramatically increased total energy dissipation (not shown). These results are consistent with the mode structure analyses in §§ 3–5.

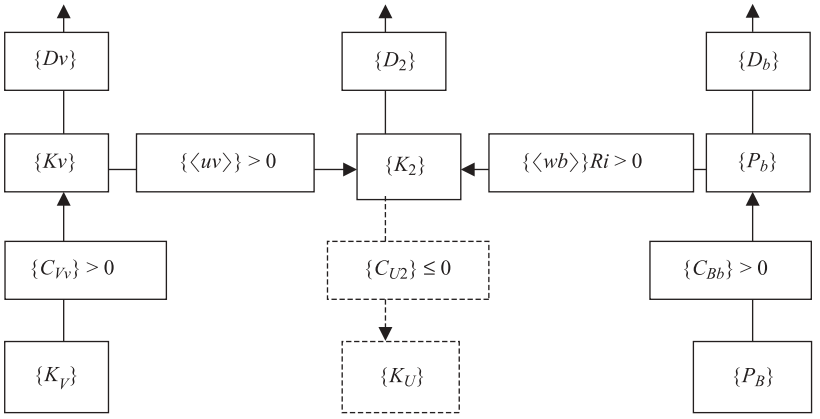

FIGURE 15. Energy conversion diagram for the nearly symmetric modes in the vicinity of the global maximum. Here, $\{P_B\}$ is the volume-averaged potential energy associated with the basic-state buoyancy, $\{K_U\}$ and $\{K_V\}$ are the volume-averaged kinetic energy components associated with the cross-band basic flow and along-band basic flow, respectively. The remaining symbols are as in (2.6)–(2.8). Note that $\{C_{U2}\}=\{K_U\}=0$ for $\alpha=0$, so the dashed part vanishes for the symmetric modes.

7.2. *Energy for the baroclinic and nearly baroclinic modes*

As explained in § 6.4, the baroclinic-type energy conversion requires both $\{\langle wb\rangle\}Ri$ and $\{\langle vb\rangle\}\sin\alpha$ be positive. Under this condition, the first energy conversion term is negative in (2.6*c*). Since $\cos\alpha=0$ for the baroclinic modes, the second energy conversion terms vanish in (2.6*a*) and (2.6*c*). Thus, $-\{\langle uv\rangle\}$ is the only energy conversion term in (2.6*b*), so it should be positive to support the growth of the baroclinic mode. The third energy conversion term in (2.6*c*) reduces to $\{\langle vb\rangle\}\mathrm{sgn}\alpha$ (for $\alpha=\pm 90^\circ$) and it should be sufficiently large to ensure that the sum of the conversion terms be positive to support the growth of the baroclinic mode. The signs of the energy conversion terms in (2.6) are thus all determined except for the third energy conversion term in (2.6*a*). The determined signs are verified by the computed energy conversions for the non-slip baroclinic mode at the conditional maximum point of $(l,\alpha)=(3.12,-90^\circ)$ (see the values at $\alpha=-90^\circ$ in figure 16*a*). The energy conversions for the baroclinic modes in the vicinity of the conditional maximum are shown by the solid boxes of the diagram in figure 17.

The growth rate pattern for the non-slip case in figure 2(*c*) of part 1 covers the range $-137^\circ\leqslant\alpha<-7^\circ$ or, equivalently, $43^\circ\leqslant\alpha<187^\circ$. As shown in figure 16(*a*), along the ridge (conditional maximum for fixed α) of this growth rate pattern, the energy conversions have the same signs as those for the baroclinic mode at $\alpha=-90^\circ$, although $\{C_{U2}\}=-\{\langle uw\rangle\}\sin\alpha$ changes sign around zero from slightly negative to slightly positive, $-\{\langle vw\rangle\}\cos\alpha$ and $-\{\langle ub\rangle\}\cos\alpha$ are no longer zero. The energy conversions for the non-slip nearly baroclinic modes in the vicinity of the global maximum are summarized in figure 17.

The growth rate pattern for the free-slip case in figure 1(*e*) of part 1 covers the range $-173^\circ\leqslant\alpha<-1^\circ$ or, equivalently, $7^\circ\leqslant\alpha<181^\circ$. As shown in figure 16(*b*), along the ridge of this growth rate pattern, $\{\langle vb\rangle\}\sin\alpha-\{\langle ub\rangle\}\cos\alpha$ is positive as in figure 16(*a*) and all the remaining terms have the same signs as those in figure 16(*a*). The energy conversion diagram is shown in figure 17. As shown by the energy dissipation curves in figure 16(*a*, *b*), the total energy dissipation is stronger for the

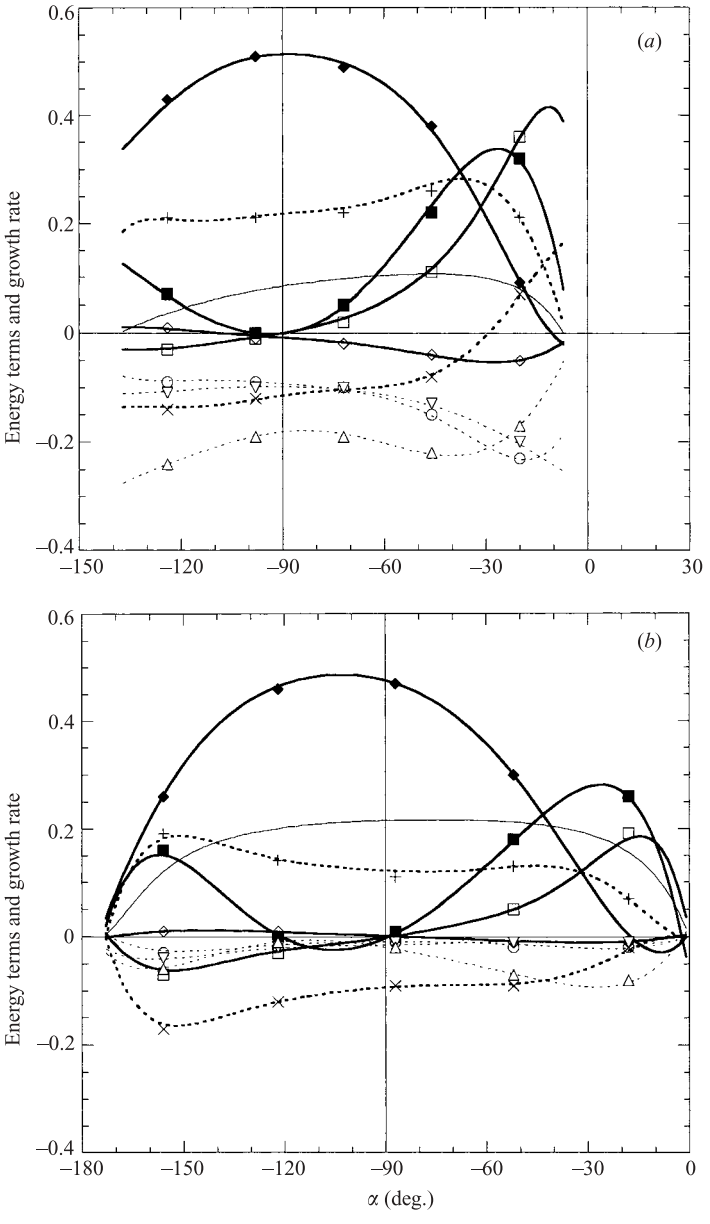

FIGURE 16. Volume-averaged energy terms in (2.6) plotted as functions of α (*a*) for the non-slip nearly baroclinic modes along the ridge (conditional maximum with α fixed) of the growth rate pattern in figure 2(*c*) of part 1, and (*b*) for the free-slip nearly baroclinic modes along the ridge of the growth rate pattern in figure 1(*e*) of part 1. The range of conditional maximum ($\sigma \geqslant 0$) is $-137^\circ \leqslant \alpha < -7^\circ$ or, equivalently, $43^\circ \leqslant \alpha < 187^\circ$ in (*a*), and is $-173^\circ \leqslant \alpha < -1^\circ$ or, equivalently, $7^\circ \leqslant \alpha < 181^\circ$ in (*b*). The external parameter values are $Ri = 1.0$, $Ek = 0.01$, $Pr = 1.0$ and $r^2 = 0.02$. Symbols as in figure 14.

non-slip case than for the free-slip case. This explains why the growth rate curve is higher and more symmetric with respect to the baroclinic point at $\alpha = -90^\circ$ for the free-slip case in figure 16(*b*) than for the non-slip case in figure 16(*a*).

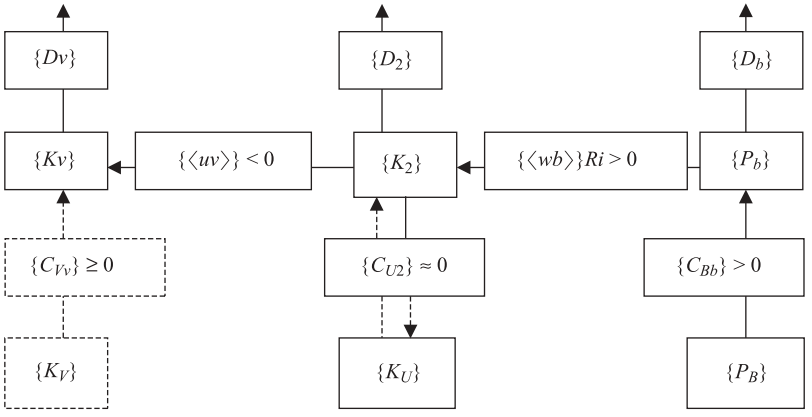

FIGURE 17. As in figure 15 but for the nearly baroclinic modes in the vicinity of the global maximum. Note that $\{C_{Vv}\}=\{K_V\}=0$ for $\alpha=\pm 90°$, so the dashed part vanishes for the baroclinic modes. The solid (dashed) arrow between $\{K_U\}$ and $\{K_2\}$ indicates that the energy conversion $\{C_{U2}\}$ is nearly zero and slightly negative (positive) for the baroclinic modes (for the nearly baroclinic modes in the vicinity of the global maximum).

8. Summary remarks

It is well known that the banded structure of the most unstable symmetric mode tends to become infinitely narrow in the inviscid limit (Fjortoft 1944; Ooyama 1966; Stone 1966). The presence of diffusivity prevents the bands from becoming infinitely narrow and thus provides a selection mechanism for the horizontal scale of the most unstable mode. This selection mechanism is intuitive and well-studied (Emanuel 1979, 1985; Miller 1984, 1985; Xu & Clark 1985; Xu 1987). The presence of diffusivity also provides a selection mechanism for the horizontal orientation of the most unstable mode with respect to the basic-flow shear (Miller & Antar 1986; part 1). This orientation selection mechanism is complex and needs to be interpreted through several steps of reasoning based on the scale selection mechanism and the results obtained in this paper. (i) The most unstable mode has a finite horizontal wavelength in the presence of diffusivity. (ii) When the horizontal wavelength is fixed at a finite value, the growth of the warm-side (or cold-side) tilted mode is maximally supported by the symmetric-type energy conversion plus the baroclinic-type energy conversion in the middle layer (or boundary layers). This explains why with the fixed finite horizontal wavelength the inviscid growth rate is conditionally maximized when the band orientation is tilted slightly to either the warm side or cold side of the basic shear. (iii) As the baroclinic-type energy conversion enhances the middle-layer (or boundary) structures of the warm-side (or cold-side) tilted mode, the mode structures are smoothed (or sharpened) near the boundaries (see §§4.2 and 5.2). Hence, the warm-side tilted mode is much (or slightly) less severely damped by the increased diffusivity than the cold-side tilted mode with the non-slip (or free-slip) boundary conditions. The above three-step reasoning provides a physical interpretation for the orientation selection mechanism. In particular, it explains why the global maximum point in the growth rate pattern (obtained with Ri between 0.25 and the inviscid transitional Richardson number $Ri^*=0.95$) shifts away from the symmetric axis to the negative side (for the warm-side tilted modes) and why the growth rate pattern on the positive side of the symmetric axis drops below zero for the non-slip case but not

for the free-slip case as the diffusivity increases (from $Ek = 0.0001$ to 0.01) (compare figures 1*a* and 2*a* of part 1 with figure 1 in this paper).

As explained in § 3.2, the symmetric-type energy conversion is characterized by conversions of perturbation energy from the perturbation along-band velocity and buoyancy to the cross-band circulation. This characterization implies two conditions. (i) The perturbation along-band velocity and buoyancy need to be supported by energy conversions from the basic-state along-band velocity and basic-state buoyancy, respectively, while the latter two conversions should be larger than the above two perturbation energy conversions, respectively (see (2.6*b*, *c*) and figure 15). (ii) The perturbation along-band velocity and buoyancy should be positively correlated with the horizontal and vertical velocity components of the cross-band circulation, respectively, in order to produce the perturbation energy conversions characterized above. This second condition further implies that the horizontal and vertical motions in the cross-band vertical plane must be accelerated by the Coriolis force associated with the perturbation along-band velocity and by the perturbation buoyancy, respectively. For the nearly symmetric modes, the perturbation Coriolis force and buoyancy are generated mainly by the cross-band advections of the basic-state along-band absolute-momentum M and basic-state buoyancy B, respectively, so the above accelerations are possible only when the perturbation parcel trajectories are steeper than the M-surface and less steep than the B-surface in the cross-band vertical plane. These features and related positive feedback are illustrated and interpreted with detailed structure and energy analyses for the symmetric modes in § 3 and for the nearly symmetric modes in §§ 4 and 5.

The baroclinic-type energy conversion is characterized by energy conversions from the basic-state buoyancy through the along-band horizontal advection to the perturbation buoyancy and then to the cross-band circulation. This characterization implies two conditions. (i) The perturbation buoyancy needs to be supported by the energy conversion from the basic-state buoyancy that is larger than the energy conversion from the perturbation buoyancy to the cross-band circulation (see (2.6*c*) and figure 17). (ii) The vertical and horizontal perturbation motions in the along-band vertical plane should both be negatively correlated with the perturbation buoyancy in order to produce the energy conversions characterized above (to ensure both $-\{\langle wb\rangle\}Ri$ and $\{\langle vb\rangle\}\sin\alpha$ are positive in (2.6*c*)). This second condition further implies that the perturbation transports warm air northward with rising motion and transports cold air southward with sinking motion, which is an essential feature for the growth of the classic baroclinic waves (§ 9.3 of Holton 1979). These features and related positive feedback are illustrated and interpreted with detailed structure and energy analyses for the baroclinic modes in § 6.4 and for the nearly baroclinic modes in §§ 6.1–6.3 and 6.5.

For the nearly baroclinic modes, the perturbation buoyancy is generated mainly by the vertical and along-band advection of the basic-state buoyancy, so the second condition implied by the baroclinic-type energy conversion also implies that the perturbation parcel trajectories must be less steep than the basic-state potential temperature surfaces in the along-band vertical plane. While the growth of the nearly baroclinic modes is supported by the baroclinic-type energy conversion, it is also assisted by two additional energy conversions: (i) from the basic-state buoyancy through the cross-band horizontal advection to the perturbation buoyancy, and (ii) from the basic-state along-band velocity to the perturbation along-band velocity. These two additional energy conversions smooth (or sharpen) the near-boundary structures of the warm-side (or cold-side) tilted nearly baroclinic mode in the inviscid

limit. Because of this, the warm-side tilted mode is less severely damped than the cold-side tilted mode by the increased diffusivity, especially with the non-slip boundary conditions. This explains why the global maximum point in the growth rate pattern (obtained with Ri larger than the inviscid transitional Richardson number $Ri^* = 0.95$) is shifted to the positive side ($\alpha > -90^\circ$) of the baroclinic axis ($\alpha = -90^\circ$) as the diffusivity increases (to $Ek = 0.01$) (see figure 1*e* or 2*c* of part 1).

The author is grateful to Drs Wei Gu and Ting Lei for developing the spectral model. The work was supported by the NSF Grant ATM-9983077 to the University of Oklahoma. Comments and suggestions from Dr Robert Davies-Jones and the anonymous reviewers improved the presentation of the results.

REFERENCES

Emanuel, K. A. 1979 Inertial instability and mesoscale convective systems. Part I: Linear theory of inertial instability in rotating viscous fluids. *J. Atmos. Sci.* **36**, 2425–2449.

Emanuel, K. A. 1983 The Lagrangian parcel dynamics of moist symmetric instability. *J. Atmos. Sci.* **40**, 2368–2376.

Emanuel, K. A. 1985 Comments on "Inertial Instability and Mesoscale Convective Systems. Part I". *J. Atmos. Sci.* **42**, 747–752.

Fjortoft, R. 1944 On the frontogenesis and cyclogenesis in the atmosphere. Part I. On the stability of the stationary circular vortex. *Geofys. Publ.* **16**, No. 5, 28 pp.

Holton, J. R. 1979 *An Introduction to Dynamic Meteorology*, Second Edn. Academic.

Miller, T. L. 1984 The structures and energetics of fully nonlinear symmetric baroclinic waves. *J. Fluid Mech.* **142**, 343–362.

Miller, T. L. 1985 On the energetics and nonhydrostatic aspects of symmetric baroclinic instability. *J. Atmos. Sci.* **42**, 203–211.

Miller, T. L. & Antar, B. N. 1986 Viscous nongeostrophic baroclinic instability. *J. Atmos. Sci.* **43**, 329–338.

Ooyama, K. 1966 On the stability of the baroclinic circular vortex: a sufficient criterion for instability. *J. Atmos. Sci.* **23**, 43–53.

Stone, P. H. 1966 On non-geostrophic baroclinic stability. *J. Atmos. Sci.* **23**, 390–400.

Stone, P. H. 1970 On non-geostrophic baroclinic stability: Part II. *J. Atmos. Sci.* **27**, 721–726.

Xu, Q. 1986 Generalized energetics for linear and nonlinear symmetric instabilities. *J. Atmos. Sci.* **43**, 972–984.

Xu, Q. 1987 The existence and stability of steady circulations in a conditionally symmetrically unstable basic flow. *J. Atmos. Sci.* **44**, 3020–3029.

Xu, Q. 2003 Nearly symmetric and nearly baroclinic instabilities in the presence of diffusivity. Part 1. Growth rate patterns. *J. Fluid Mech.* **492**, 181–205.

Xu, Q. & Clark, J. H. E. 1985 The nature of symmetric instability and its similarity to convective and inertial instability. *J. Atmos. Sci.* **42**, 2880–2883.